Article:
Pommier, A., Tauber, M.J., Renggli, C. et al. (2 more authors) (2025) Electrical Properties of Alkaline Earth Sulfides and Implications for the Interior of Mercury. Journal of Geophysical Research Planets, 130 (2). e2024JE008651. ISSN 2169-9097

https://doi.org/10.1029/2024je008651

Electrical Properties of Alkaline Earth Sulfides and Implications for the Interior of Mercury

Anne Pommier[1*], Michael J. Tauber[1,2], Christian Renggli[3], Christopher Davies[4], Alfred Wilson[4]

[1] Carnegie Institution for Science, Earth and Planetary Laboratory, Washington DC, USA

[2] University of San Diego, Department of Chemistry and Biochemistry, San Diego CA, USA

[3] Max Planck Institute for Solar System Research, Göttingen, Germany

[4] University of Leeds, School of Earth and Environment, Leeds, UK

* Corresponding author. Email: apommier@carnegiescience.edu

Abstract

Alkaline earth sulfides are possibly abundant in the mantle of Mercury, and knowledge of their melting and transport properties is needed to investigate the structure of the planet. We report electrical experiments at pressures in the range 2 – 5 GPa and at temperatures up to ~2400 K on analogs of natural sulfides, i.e., impurity-bearing $Ca_{1-x}Mg_xS$. Electrical conductivity increases nonuniformly with temperature, with no systematic dependence on cation composition. Below 1700 K, the conductivities span a wide range, whereas at higher temperatures the values converge within ~0.5 – 7 S/m at 1800 K and 5 GPa. The conductivity trends are complex, and reflect contributions from divalent cations, alkali metal and carbon impurities, which would similarly contribute to the conductivity of Mercury's crust and mantle. Melting is identified by a jump in conductivity, occurring between ~1850 and 2100 K at 5 GPa. These low temperatures are consistent with the presence of impurities. Using electrical studies on relevant silicate minerals and petrological observations, we develop electrical conductivity-depth profiles of Mercury's mantle. Depending on the interconnectivity of the sulfide phase, the conductivity at the base of the mantle containing 8 vol.% sulfide ranges from ~0.2 to > 8 S/m. Our results can be tested with future observations from the ESA-JAXA Bepi-Colombo mission.

Plain language summary

(Ca,Mg)S are possibly abundant in planet Mercury, and their study can provide important information about the interior of the planet. We performed electrical experiments under relevant pressure and temperature conditions on analogs of natural (Ca,Mg)S. Conductivity increases with temperature, with no systematic effect of composition. The complex electrical response reflects contributions from cations and carbon impurities, as expected in natural rocks in Mercury. Melting is identified from the electrical measurements and happens at low temperatures due to the presence impurities. Using our results and previous studies, we develop electrical conductivity-depth profiles of Mercury's mantle. The conductivity at the base of the mantle depends strongly on the connectivity of the sulfide. Our models can be compared with future observations from the Bepi-Colombo space mission to Mercury.

Keywords: Mercury, alkaline earth sulfide, impurities, impedance spectroscopy, electrical conductivity, Raman spectroscopy, melting.

Keypoints

- Electrical experiments were performed at 2 and 5 GPa and up to ~2400 K on analogs of natural Ca-Mg sulfides
- Melting is characterized by a jump in conductivity and occurs between ~1850 and 2100 K at 5 GPa
- Depending on sulfide interconnectivity, the conductivity of Mercury's CMB containing 8 vol.% sulfide ranges from ~0.2 to > 8 S/m

1. Introduction

Alkaline earth sulfides are present in some extraterrestrial materials under highly reducing conditions (e.g., Avril et al., 2013). For Mercury in particular, several lines of evidence support the presence of $Ca_{1-x}Mg_xS$ in the silicate portion of the planet. First, spectroscopic analyses of the surface are consistent with highly reducing conditions, low Fe content, and an abundance of sulfides in the oldhamite (CaS) - niningerite (MgS) system (e.g., Burbine et al, 2002; Stockstill-Cahill et al., 2012; Vilas et al., 2016). Second, alkaline earth sulfides are commonly observed in enstatite chondrites or aubrites, and these meteorites are thought to represent building blocks of Mercury (Crozaz and Lundberg, 1995; Burbine et al., 2002 and references therein; Lehner et al., 2013; Cartier and Wood, 2019). Third, alkaline earth sulfides are expected to form during the cooling of a Fe-poor, reduced magma ocean. Several laboratory studies on analogs of the Hermean magma ocean and mantle at relevant pressure and temperature conditions have revealed the presence of (Ca,Mg,Fe)S phases (e.g., Namur et al., 2016a; Boukaré et al., 2019; Anzures et al., 2020). Depending on the density contrast between these sulfides and the surrounding silicate phases, as well as the mobility (viscosity) of sulfides at depth, $Ca_{1-x}Mg_xS$ could have migrated upward or remained at the depth they formed, leading to sulfide-rich and sulfide-poor regions in the mantle (e.g., Boukaré et al., 2019).

Although the abundance of sulfides in the silicate portion of the planet remains largely unknown, melting experiments on the Indarch EH chondrite showed the presence of several vol.% sulfides, likely CaS and MgS (Burbine et al., 2002). Stockstill-Cahill et al. (2012) estimated the abundance of sulfides to be 8 wt.% for Indarch, ~2 wt.% for the northern volcanic plains (NVP), and ~3 wt.% for the intercrater plains and heavily cratered terrain (IcP-HCT). Using existing field observations and petrological modeling, Lark et al. (2022) calculated that the mantle could contain up to 13–20 wt.% low density (Ca,Mg) sulfides. In a heterogenous mantle, these estimates open the possibility that sulfide-rich regions are partially interconnected, thereby affecting the transport properties of the mantle. For instance, it has been shown that even a partial network of solid or molten FeS in a silicate matrix strongly influences bulk electrical conductivity (e.g., Yoshino et al., 2003, 2004; Watson and Roberts, 2011; Tauber et al., 2023).

To understand the impact of $Ca_{1-x}Mg_xS$ compounds on the transport properties of a heterogeneous mantle, it is first necessary to know the properties of the alkaline earth sulfides in isolation. Our knowledge of the chemical and physical properties of $Ca_{1-x}Mg_xS$ compounds derives

largely from studies performed at atmospheric pressure, and with applications mainly on the luminescence of these materials (e.g., Pandey and Sivaraman, 1991 and references therein; Collins and Ling, 1993). At 1 atm pressure, alkaline earth sulfides are characterized by a face-centered cubic NaCl (halite) structure, high melting temperatures (~2300 K), and the CaS–MgS system is immiscible below ~1473 K (Skinner and Luce, 1971; Dilner, 2016). Under pressure (several tens of GPa), theory and experiments indicate that the halite structure remains the most stable one for CaS and MgS (e.g., Luo et al., 1994; Jha et al., 1998). However, experimental studies of $Ca_{1-x}Mg_xS$ at high pressure and temperature conditions relevant to Mercury are scarce, and their stability field at the mantle conditions, as well as their physical (transport) properties, remain to be understood. One explanation resides in the fact that both the synthesis of $Ca_{1-x}Mg_xS$ compounds in the laboratory and their study in large-volume presses is challenging because of reactions with atmospheric oxygen and water.

Electrical conductivity is a fundamental transport property to investigate the present-day interior structure of planet Mercury. Using electromagnetic induction, previous space missions have detected conducting materials (e.g., metallic core, magma, subsurface ocean) that are part of the layered structure of terrestrial bodies (e.g., Dyal and Parkin, 1971; Kivelson et al., 2000; Khurana et al., 2011). Given the sensitivity of conductivity on temperature, electrical observations can also provide clues about the thermal state of a planet or moon. As a result, determining the electrical conductivity-depth profile of Mercury is an important science objective of the ESA-JAXA Bepi-Colombo mission (Verhoeven et al., 2009; Genova et al., 2021). Inferring the presence and distribution of alkaline earth sulfides in Mercury based on electromagnetic measurements in space still requires laboratory-based measurements of their electrical properties. Previous electrical studies of $Ca_{1-x}Mg_xS$ compounds are limited, focusing mostly on CaS and MgS endmembers at 1 atm pressure (**Figure 1**). CaS and MgS are wide bandgap semiconductors. The electrical conductivity of pure samples is typically dominated by metal cations (e.g., Nakamura et al., 1995). At a given temperature, the electrical conductivity of CaS is comparable to that of MgS (Egami et al., 1981; Nakamura et al., 1995), and significantly lower than that of FeS (e.g., Pommier, 2018; Littleton et al., 2021). At 1 atm pressure, and at temperatures up to 1200 K, Nakamura and Gunji (1980) highlighted the importance of impurities on the electrical properties of CaS, with electrical conductivity increasing at least 10 times when synthesized in a graphite or alumina container rather than in a CaS container. Graphite impurities are particularly relevant to natural sulfides in Mercury,

given the abundance of carbon in the planet (e.g., Peplowski et al., 2016; Charlier and Namur, 2019).

Electrical experiments in the laboratory can also contribute to evolutionary models of planet Mercury. Specifically, to model the cooling of a sulfide-bearing mantle naturally requires that the temperatures of relevant liquid/solid phase transitions be known. Impedance spectroscopy can be used to detect these transitions *in situ* under controlled conditions. For example, at 6 GPa, a dramatic conductivity jump was observed for commercial CaS at ~2400 K, a clear indicator of melting at this pressure (Pommier et al., 2019). Analogous measurements on various $Ca_{1-x}Mg_xS$ compounds, at pressures relevant for Mercury's mantle, have yet to be reported.

In this study, we investigate the electrical properties of polycrystalline $Ca_{1-x}Mg_xS$ at pressure and temperature conditions relevant to the mantle of Mercury. The synthesis of these sulfides in graphite capsules adds C impurities and enhances the connection to Mercury's mantle where significant carbon has been reported. We performed electrical experiments on the different samples using impedance spectroscopy at 2 and 5 GPa and up to ~2200 K. Electron microprobe and Raman/IR analyses complement the characterization of the samples. These results are used to develop electrical conductivity-depth profiles of the sulfide-bearing mantle that can be compared with data anticipated from the Bepi-Colombo mission.

2. Experimental methods

2.1. Sample preparation

Starting mixtures were prepared from chemical grade $CaCO_3$ and MgO powders. The MgO powder was fired at 1273 K for 2 h and then stored in a drying oven at 393 K. The $CaCO_3$ powder was decarbonated at 1273 K for 8 h. Different proportions of CaO and MgO powders were mixed to obtain six compositions. The oxide mixtures were homogenized in an agate mortar with ethanol solvent for 30–40 minutes. For each composition, 0.03 g of oxide mixture was loaded into a graphite cup with an outer diameter of 4 mm and an inner diameter of 3 mm. Elemental S was placed in a second graphite cup with similar dimensions. The amount of S was weighed to obtain a molar ratio of (Ca+Mg)/S = 0.6. The excess S was chosen to ensure complete conversion of the oxides to sulfide according to the reaction:

$$Ca_xMg_{1-x}O + S(g) + C = Ca_xMg_{1-x}S + CO(g) \quad (1)$$

The two graphite cups were stacked in a silica tube (4-mm ID, 4 – 5-cm length) that was sealed under vacuum using a H_2–O_2 torch and placed in a vertical tube furnace at 1473 K for 24 h (Renggli et al., 2022, 2023; Reitze et al., 2024). This temperature is close to, but above, that of the solvus of the CaS–MgS system (Skinner and Luce, 1971). Samples were quenched by dropping the silica tubes in cold water. The quenching rate is estimated to be >200–300 K/s. Upon opening the silica tubes, the production of sulfide aggregates was apparent, and CO was detected. Six compositions were synthesized: CaS, $Ca_{0.8}Mg_{0.2}S$, $Ca_{0.6}Mg_{0.4}S$, $Ca_{0.4}Mg_{0.6}S$, $Ca_{0.2}Mg_{0.8}S$, and MgS. The sulfides were mineralogically and spectroscopically characterized as described below. The starting materials are expected to contain small amounts of carbon, resulting from the synthesis in graphite capsules. The presence of carbon is relevant to Mercury because significant quantities of this element are present in this planet (up to 5 wt.% in low reflectance crustal materials; Peplowski et al., 2016). The samples were crushed into a powder using an agate mortar and pestle within a nitrogen-filled glovebox. For comparison, a CaS powder from ThermoFisher (99.9% purity) was added as one of the starting materials. This commercial powder contains ~500 ppm Sr and ~0.1 % different elements (mostly Na, K, and trace amounts (<0.001%) of Mg, Ba). Sulfide powders were stored in a desiccator until used in electrical experiments.

2.2. Impedance spectroscopy measurements under pressure and temperature

Electrical experiments were carried out on the six lab-synthesized sulfide powders in the CaS-MgS solid solution, as well as the commercial CaS powder, at 2 and 5 GPa under quasi-hydrostatic conditions in a Walker-type multi-anvil press (Rockland; 1,100-ton). Two previous experiments on a CaS powder from Alfa Aesar at 3 and 6 GPa (experiments BB175 and BB 177; Pommier et al., 2019) are added to the electrical dataset. Experimental conditions are listed in **Table 1**. Pressure was applied using eight tungsten carbide cubes with corner-truncated edge length of 8 mm and MgO octahedral pressure media with an edge length of 14 mm. All MgO parts were fired at ≥1273 K and stored in a desiccator until use. The electrical cell assembly consisted of three MgO sleeves, with the middle one comprised of three alumina rings separated from each other by two high-purity Ta or Mo disks (**Supplementary Figure S1**). Both Ta and Mo have extremely high melting points, and are suitable for low oxygen environments such as present in this cell assembly. The use of two different metals allows the effect of electrode contamination on the

electrical response to be probed. The middle alumina ring contained the sample, and the design prevented molten material from escaping the cell (e.g., Pommier et al., 2023).

The sample was heated by applying a current to the surrounding Re foil, and temperature was monitored using one of two Type-C thermocouples ($W_{95}Re_5$-$W_{74}Re_{26}$). Each thermocouple contacted one of the two metal disks that served as electrodes for impedance measurements. The cell assembly was initially compressed to the target pressure at room temperature, and the temperature was then increased in 25 K increments. Each sample was annealed at a temperature that is significantly below the expected melting point of the sulfides (typically, 2–3 h at 873–1073 K and 0.5–1h at 1473 K). The annealing ended after a relatively steady resistance value was obtained. The stabilization in bulk resistance is interpreted as the attainment of a certain degree of textural and chemical equilibrium. Annealing times longer than a few hours were avoided to minimize possible oxidation of the sample. Impedance data were collected during subsequent heating. **Supplementary Figure S2** shows the temperature–power paths for all experiments. The pressure remained within (±) 2% of the target value throughout the heating cycle. For two experiments (BBC83 and BBC85), the electrical response of the sample was first measured at 2 GPa (BBC83) or 5 GPa (BBC85) at temperatures below the melting point (up to 1573 K or less), then measured at 5 GPa (BBC83) or 2 GPa (BBC85) over a wide range of temperature. Measurements at the first pressure were performed at temperatures below the melting point of the sample, so that the initial measurements at the second pressure are not affected by melting. Electrical measurements during heating and cooling cycles were reproducible at both pressures (**Supplementary Figure S3**). All experiments were quenched by turning off the power to the heater. After decompression, the electrical cell was mounted in an epoxy resin, sliced longitudinally, and polished without water to expose the surface of the sample for chemical and textural microprobe analyses. The mounted samples were stored in a desiccator until analyses.

Electrical measurements consisted of 4-electrode impedance spectroscopy (Ametek 1260 Solartron Impedance/Gain-Phase Analyzer). To measure the complex impedance, a potential with DC component 0.1 or 1 V and AC amplitude ≤ 1 V was applied from 5 MHz to ~1 Hz. The sample response was not sensitive to variation in AC amplitude between 500 mV and 1 V. The value of the real part of the complex impedance is determined at relatively low frequency, either as a local minimum in the complex impedance plane, otherwise as an intersection or extrapolated intersection with the real axis and is considered the bulk electrical resistance (R) (**Supplementary**

Figure S4). The sample resistance R_{sample} is obtained from R after removing very minor contributions from the alumina sample ring and the two electrode disks. Reproducibility was checked by (1) making multiple measurements during an experiment at defined temperature, and (2) duplicating electrical experiments for one composition ($Ca_{0.8}Mg_{0.2}S$) at 5 GPa and overlapping temperature ranges. The electrical conductivity σ of the sample at defined temperature is calculated from R_{sample}:

$$\sigma = \frac{1}{R_{sample} \times G} \quad (2)$$

with G the geometric factor, corresponding to $\pi r^2/l$ (electrode disk area/sample thickness). The error in each conductivity value is typically a few percent (**Supplementary Information**).

2.3. Sample analyses

Starting powders and quenched samples retrieved after electrical experiments were analyzed using the electron microprobe to characterize the composition and texture. Analyses were performed with a JEOL 8530F field-emission electron microprobe at Carnegie Science, with an acceleration voltage of 15 kV and a sample current of 15 or 30 nA. Integration times were 20 s on peak and 10 s on background, except for Na and K (10 s and 5 s, respectively). The beam diameter was 1 μm. Ca, Mg, and S were measured using anorthite, olivine, and pyrite standards, respectively. Potential contamination from the synthesis or the multi-anvil cell parts was checked using the following standards: tantalum metal (Ta), molybdenum metal (Mo), pyrite (for Fe), anorthite (Al), olivine (Si), ilmenite (Mn), orthoclase (K), and albite (Na). In addition to spot analyses, energy dispersive spectroscopy (EDS) and wavelength dispersive spectroscopy (WDS) using a 1-μm diameter beam and a 20-ms dwell time were used to obtain chemical maps of selected quenched samples.

Raman spectroscopy was performed on three starting sulfide powders (lab-synthesized CaS, $Ca_{0.6}Mg_{0.4}S$, and $Ca_{0.2}Mg_{0.8}S$), primarily to identify impurities. The spectra were acquired with samples at ambient conditions in open air with low humidity. A customized microscope system was employed (see **Supporting Information** for details). Excitation wavelengths were 514.53 nm and 647.09 nm, and each spectrum was acquired over a period of several minutes. At the sample, the power of the 514.5-nm beam was 0.3 or 0.6 mW, and the focus was circular with diameter ~1 μm. Therefore, each spectrum with 514.5-nm excitation probed a small portion of one grain. For 647.1 nm excitation, the beam power was ~4 mW at the sample, and the shape was

elliptical (3 μm × 300 μm) to lower the irradiance by several orders of magnitude, and to analyze a much larger portion of each sample during a given acquisition. For these spectra, a row of powder grains was probed simultaneously. The spectral window covered Raman shifts from 500–1660 cm^{-1}, selected to monitor Raman scattering from various suspected impurities rather than the first-order bands (<500 cm^{-1}) from phonons of $Ca_{1-x}Mg_xS$. The spectra excited with 647.09-nm light were calibrated to an accuracy of ±1 cm^{-1}, and corrected for the instrument response by acquiring the spectrum of a reference fluorophore. Mid-infrared spectroscopy analyses of the lab-synthesized starting materials (Reitze et al., 2024) have been added to the dataset.

3. Results

3.1. Chemical analyses

3.1.1. Analysis of starting powders

Electron microprobe analysis and crystallography: The chemical compositions of starting materials based on electron microprobe analyses are presented in **Table 2**. The results are in very good agreement with the targeted compositions. The lattice parameters for the six samples vary in proportion to the amount of Ca and Mg, from 5.21 Å (MgS) to 5.69 Å (CaS) (Reitze et al., 2024). This finding is consistent with prior reports (Collins and Ling, 1993; Kasano et al., 1984) and implies CaS–MgS forms a solid solution at the temperature of our synthesis. The CaS material contains oxidized regions characterized by a low total (88.8 wt.%).

Raman spectroscopy: Representative spectra of lab-synthesized CaS acquired with 514.5-nm excitation and circular focus are shown in **Figure 2**, after subtracting a background caused by luminescence. The spectrum has Raman bands with peak positions near 160, 180, and 200 cm^{-1}. These peak positions are similar to those reported previously for CaS (Avril et al., 2013; Gyakwaa et al., 2020). For the samples with 0.4 or 0.8 fractional Mg, the luminescence was much higher, and overwhelmed any Raman signals (spectra not shown).

Raman spectra in the impurity region acquired with 647.1-nm excitation are shown in **Figure 2**, after correction for the instrument response and subtraction of a background. The spectra of samples containing Mg exhibit much lower luminescence than with 514.5-nm excitation. Among the three samples, only the lab-synthesized CaS shows evidence of a sulfur-oxide impurity, with a band at 1002 cm^{-1} that is also observed in a spectrum acquired with 514.5-nm excitation.

The highest amplitude feature in the CaS spectrum is a broad band centered at 1124 cm^{-1}, likely caused by luminescence from trace amounts of chromium (see Discussion). The broad feature at 1168 cm^{-1} in the spectrum of $Ca_{0.6}Mg_{0.4}S$ may have the same origin. The 647.1-nm Raman spectrum of $Ca_{0.6}Mg_{0.4}S$ also has significant bands centered at 1335 and 1590 cm^{-1}, and analogous (though smaller) features are observed for the CaS sample. As discussed below, these bands are assigned to graphitic carbon. The Raman spectrum of the $Ca_{0.2}Mg_{0.8}S$ sample is relatively featureless, and does not show clear signatures of oxidation, chromium, or carbon.

Mid-infrared spectroscopy: Reflectance spectra of the lab-synthesized samples over the range 7 – 12.5 μm (800 – 1430 cm^{-1}) are shown in **Supplementary Figure S5**. Frequencies in this spectral region exceed those of first-order phonon resonances for alkaline-earth sulfides. Therefore, absorption or transmission spectra of pure CaS and MgS should lack features in this window (e.g., spectrum of CaS in Madarász et al., 1996; comment regarding CaS and MgS on pg. 26 of Hofmeister et al., 2003), and corresponding reflectance spectra are expected or known to lack reststrahlen or other bands (e.g., see reflectance spectrum of $Mg_{0.9}Fe_{0.1}S$ in Mutschke et al., 1994). The spectra presented in **Supplementary Figure S5** largely agree with this expectation and prior work, except for the spectrum of CaS. The impurities associated with this mid-IR spectrum are discussed briefly below and are presented more comprehensively in Reitze et al. (2024).

3.1.2. Analysis of samples after electrical experiments

Electron microprobe analyses of quenched samples after electrical experiments are listed in **Table 2.** Examples of texture and WDS maps are shown in **Supplementary Figure S7** and traverses on selected samples are shown in **Figure 3**. Our analyses are in broad agreement with the starting compositions, though Mg and S content tends to be slightly lower than in the starting materials. Totals for the retrieved samples can be as low as 95.3 wt.%, which can be explained by (1) the complex texture of quenched molten samples, including a high porosity, as well as a small grain size (**Supplementary Figure S7A**), and (2) a small degree of oxidation explains the lowered values of S content relative to starting material, likely caused by the preparation for analyses. The lowest totals are associated with the largest differences in Mg content between starting and retrieved materials, consistent with MgS reacting with oxygen to form MgO regions with a S-rich rim (<~60 μm in diameter) (**Supplementary Figure S7B**).

Contamination of the sample at high temperature from the alumina sleeve extends only over a small distance, <~40 μm (**Figure 3**). For experiments using Mo electrodes, a thin (~60 μm) Mo-S layer is observed at the sample-electrode interface, and Mo incorporates in the sample over a small range (up to ~150 μm from the Mo-S layer) (**Supplementary Figure S7C**). The use of Ta electrode disks minimizes sample rination, with small amounts of Ta present in the sample over a distance < 40 μm from the electrode (**Figure 3**). The chemical interactions between the sample and the alumina sleeve or the Mo or Ta disks are therefore limited. However, the possible presence of Al, Mo, Ta impurities in the sample at levels below the detection limit of the electron microprobe (<~0.1 wt.%) could increase bulk conductivity of the alkaline earth sulfide sample significantly, as shown at 1 atm for Al and C (Nakamura and Gunji, 1980). Back-scattered electron (BSE) images of the retrieved samples indicate that the sample diameter remained identical during the experiment, and that electrode disks sometimes deformed slightly during compression. In this case, the sample thickness considered to calculate the geometric factor G in Eq. (2) is an average value.

3.2. Impedance spectroscopy

Representative impedance spectra collected during heating after annealing are presented together with electrical conductivity values for sample $Ca_{0.2}Mg_{0.8}S$ in **Figure 4**. Three stages can be identified: at low temperature (<1500–1600 K at 5 GPa; stage 1), impedance spectra consist of an arc, and its size decreases with increasing temperature. The temperature dependence of conductivity (σ) can be reproduced satisfactorily with an Arrhenius equation

$$\sigma = \sigma_0 \times exp(\frac{-\Delta H}{RT}) \quad (3)$$

with σ_0 the pre-exponential factor, ΔH the activation enthalpy, and R the gas constant. For all samples, the activation energy in stage 1 varies from 0.8 to 1.6 eV at 5 GPa and from 0.9 to 1.9 eV at 2 GPa, with no systematic effect of composition. From ~1600 to 2000 K (stage 2), the arcs are affected by noise and only the low frequency portion is visible. Conductivity is less dependent on temperature than in stage 1. The onset of stage 3 (>2000 K) is marked by a significant jump in conductivity followed by a plateau. The resistance values are small, and the arc disappears because the complex response is dominated by inductance (positive Z") (e.g., Ni et al., 2011).

Figure 5 shows the electrical conductivity for all samples as a function of temperature. No systematic effect of composition is observed for CaS–MgS aggregates, but all samples are

significantly more resistive than FeS (by 5 log units or more at defined temperature). The lab-synthesized CaS sample is an outlier compared to all other CaS–MgS materials, with a conductivity that is at least 10 times lower than the conductivity of other samples, including commercial CaS. The activation energy of this sample at low T (0.9 eV at 2 GPa, 1.0 at 5 GPa) is similar to that of the other samples. For all samples except this CaS outlier, large variations (~3 log units) in conductivity are observed at 5 GPa and the lowest temperatures, and conductivity values tend to converge towards a narrower conductivity range as temperature increases. Each composition is characterized by a sharp increase (up to 1000 times) in conductivity at high temperature (~1900–2200 K at 5 GPa).

Comparison between conductivity data acquired at 2 and 5 GPa shows a non-negligible effect of pressure below ~1600 K. For both experimentally synthesized CaS and $Ca_{0.2}Mg_{0.8}S$, increasing pressure decreases conductivity by a factor in the range of 10-50. This observation contrasts with commercial CaS at 3, 5, and 6 GPa, for which the conductivity tends to increase slightly with increasing pressure.

4. Discussion

4.1. Analysis of impurities

By electron microprobe analysis, the nearly 100 wt.% totals indicate that the starting materials have low levels (less than thousands ppm) of impurities. Totals as low as 95.3 wt.% are found for quenched samples, but these values are likely affected by preparation in ambient conditions prior to the analysis. Slight oxidation is expected, and consistent with the fact that it is primarily the sulfide content that is lower for the quenched samples relative to starting materials.

While electron microprobe analysis provides reassurance that the starting samples are not heavily contaminated, the possibility remains that lesser impurities could affect electrical measurements (Nakamura and Gunji, 1980). Therefore, we have attempted to probe possible impurities with vibrational spectroscopy. The first Raman spectroscopic study of $Ca_{1-x}Mg_xS$ solids with halite structure (Avril et al., 2013) expressed an important point: despite selection rules forbidding first-order Raman scattering from crystals with this structure, impurities and defects can circumvent these rules and allow bands to appear. Our 514.5-nm spectra of lab-synthesized CaS showing three bands with peak positions similar to those reported by Avril et al. (2013) and

Gyakwaa et al. (2020) agree with this fundamental point. One difference between our study and that of Avril et al. is that Mg-bearing samples were successfully probed with Raman spectroscopy using 514.5-nm excitation in their case but not ours. Given the high sensitivity of the Raman spectrometer, it is possible that excessive emission in our case is caused by very minor quantities of impurities or defects, below the amounts that would significantly affect electrical conductivity.

Regarding possible oxide contaminants in the synthesized $Ca_{1-x}Mg_xS$ samples, it is reassuring that the combined Raman and IR spectra show no clear signatures of sulfur-oxide (sulfate or sulfite) species except in the case of CaS. For this sample, the narrow Raman band with peak position at 1002 cm^{-1} is a typical assignment for a symmetric stretch of sulfate, SO_4^{2-}. However, the specific frequency is significantly lower than previously reported for $CaSO_4$ at any level of hydration (~1017 cm^{-1} for anhydrite, 1008 cm^{-1} for gypsum; Liu, 2018; Schmid et al, 2020). Calcium sulfite can be ruled out as an alternative: although the symmetric stretch of pyramidal SO_3^{2-} with Ca^{2+} cation is known to have a Raman shift very close to 1000 cm^{-1} (e.g., see spectra of hannebachite $CaSO_3 \cdot 0.5H_2O$ or anhydrous $CaSO_3$ in Frost and Keeffe (2009), Lutz and El Suradi (1976)), our spectrum lacks a characteristic signature of an asymmetric stretch of SO_3^{2-} which appears in calcium samples as a second band downshifted 30–50 cm^{-1} relative to the first (Frost and Keeffe, 2009; Lutz and El Suradi, 1976). Therefore, the band at 1002 cm^{-1} in our Raman spectra is best assigned to sulfate oxidation products, and we suggest that the unusually low frequency is a consequence of $CaSO_4$ largely surrounded by unreacted CaS, a different environment than uniform anhydrous or hydrated $CaSO_4$ single crystals. In contrast to the results from Raman spectroscopy, the IR reflection spectrum (**Supplementary Figure S5**) shows no band over the range 8 – 9 μm that would support the presence of sulfate (e.g., see reflection spectra of anhydrite and gypsum in Salisbury et al., 1991). The local maxima between 10 – 11 μm may be interpreted as Reststrahlen features associated with strong absorption bands of sulfite in this region (e.g., Lutz and El Suradi, 1976; Wallace, 2024). Though a consistent assignment of the vibrational spectra to sulfate or sulfite is not possible, nevertheless we can conclude that the synthesized CaS sample has significant sulfur-oxide impurities.

The 1335 and ~1590/1600 cm^{-1} bands clearly observed with 647.1-nm excitation for $Ca_{0.6}Mg_{0.4}S$, and to a lesser extent CaS, are best assigned to graphitic carbon based on the following logic: (1) given the graphite holder of the product sample, carbon is an obvious candidate impurity; (2) we are confident that these bands are not artifacts, given careful correction for the instrument

response; (3) a pair of bands, including the G-band, in the 1580 – 1620 cm^{-1} range is typical for microcrystalline graphite (e.g., Nemanich and Solin, 1979); (4) the peak position of the lower frequency (1335 cm^{-1}) band is very close to the expected position for the highly dispersive D-band of disordered graphite-like materials with 647.1-nm (1.9-eV) excitation (Sood et al., 2001); (5) although the spectrum of CaS acquired with 514.5-nm excitation did not include analogous Raman bands that would support the presence of graphitic carbon, it is reasonable that these signatures are missing because of sample heterogeneity in combination with the very small region probed by the circularly-focused 514.5-nm beam. Additional reasons include the relatively low carbon content in the CaS sample and the low signal-to-noise ratio of the spectra collected with 514.5-nm excitation. The Raman spectra collected with 647.1 nm excitation do not allow the carbon content to be quantified, however, based on experience with other samples probed with the same spectrometer, it is likely that the amount of carbon in the $Ca_{0.6}Mg_{0.4}S$ sample is in the range 100 – 1000 ppm.

The 1124 and 1168 cm^{-1} bands for lab-synthesized CaS and $Ca_{0.6}Mg_{0.4}S$ are most likely caused by luminescence from trace chromium Cr^{3+} impurities. This assignment is based partly on the fact that these bands are not observed in the spectral window with 514.5-nm excitation. Additionally, the absolute wavenumber / wavelength positions of these bands are located at typical values for Cr^{3+} emission, i.e., 14330 or 14290 cm^{-1} (698 or 700 nm). For example, Cr^{3+} in an MgO matrix has a prominent luminescence peak at 699 nm when excited with 632.8-nm light (Schmid et al., 2021). The Raman system is very sensitive to any emitting source, therefore the amount of chromium impurity in these samples should be well below the threshold for detection by microprobe analysis. The assignments for the ~693 and ~815 cm^{-1} bands are uncertain. We considered the possible contribution of higher-order Raman scattering from the alkaline metal sulfide, however this was ruled out because the bands were not observed with 514.5-nm excitation, and second-order spectra reported for comparable alkaline-earth oxides with halite structure (Rieder et al., 1973; Buchanan et al., 1974) show a richer array of peaks with little semblance to our spectra. Sidebands in the luminescence may contribute, as seen for Cr^{3+} in MgO (e.g., Schmid et al., 2021). The difference in frequency between the two bands with peak positions at 815 and 1124 cm^{-1} that we suggest may both be caused by luminescence from Cr^{3+} is ~310 cm^{-1}, similar to a phonon frequency of 293 cm^{-1} reported for luminescence from Ce^{3+} doped in CaS (Yokono et al., 1979).

4.2. Electrical conductivity of sulfide aggregates at pressure and temperature

Our electrical results do not reveal a clear effect of sulfide chemistry (cation) on conductivity. Although CaS and MgS are both highly ionic, large-bandgap semiconductors with the same lowest-energy halite structure at all pressures of the present work, there are significant differences between the solids that give reason to expect different conductivities at a fixed temperature. First, the ionic radius of Mg^{2+} is significantly smaller than that of Ca^{2+} (0.72 Å vs 1.00 Å respectively, assuming coordination number of 6; Klein and Hurlbut, 1999). The smaller and presumably more mobile Mg^{2+} cation should imply a higher conductivity for pure MgS than CaS. Second, a fundamental difference between the alkaline sulfides is the lack of d-orbital contribution in the bonding of Mg, which causes the band structure of MgS to differ significantly relative to CaS (e.g., Farrell et al., 2002). If electron or hole transport contributes to the conductivity, as shown at some sulfur fugacities (e.g., Egami et al., 1981; Nakamura et al., 1995), these changes in band structure should impact e^-/h^+ conduction mechanisms. Electrical studies at 1 atm have shown that the conductivity of MgS is either similar or only slightly higher than that of CaS (Egami et al., 1981; **Figure 1**); therefore, for electrical conductivity measurements to distinguish these fundamental differences (and others) between MgS and CaS would require very pure samples. As others have pointed out (e.g., Nakamura and Gunji, 1980), synthesizing high-purity samples is challenging because the samples are reactive, and because their intrinsically low conductivity causes sensitivity to minor amounts of impurities including carbon, aluminum, sodium, and oxygen. Because bulk conductivity corresponds to the sum of all contributions from the different charge carriers, these impurities can mask effects due to the Ca/Mg ratio.

Trace amounts of impurities in solids can form defects in sufficient amounts to affect conductivity significantly. For instance, the addition of ~300 ppm Li^+ to the analogous ionic solid MgO increases its conductivity by a factor of ~10 (Norby and Andersen, 1991). The commercial CaS sample also contains alkali impurities (~200 ppm Na^+), which could explain the high conductivity values of this sample (**Figure 5**). In fact, Li^+ in MgO can be seen as an analog of Na^+ in CaS, given the similar ionic radii of the impurity and the alkaline earth cation (0.74 Å for Li^+ vs. 0.72 for Mg^{2+}, and 1.02 Å for Na^+ vs. 1.00 for Ca^{2+}; Klein and Hurlbut, 1999). We note that impurities in these amounts (i.e., a few hundreds of ppm) are too low to be detected using microprobe analyses.

The lab-synthesized samples were made in graphite capsules, resulting in the presence of C in the starting materials (**Figure 2**). The solubility of C in alkaline earth sulfide remains unconstrained, and graphite could be present at grain boundaries. It has been shown that for samples synthesized in graphite capsules, carbon impurities increase bulk sulfide conductivity significantly (Nakamura and Gunji, 1980). Results from our Raman spectra agree with this influence (see above): the most conductive mixed sample ($Ca_{0.6}Mg_{0.4}S$) has two bands that support the presence of graphitic carbon (**Figure 2**), whereas the least conductive mixed sample ($Ca_{0.2}Mg_{0.8}S$) did not show similar features.

The sensitivity of CaS conductivity to chemistry is evidenced with the lab-synthesized sample. As described above, the vibrational spectroscopy of this sample shows clear signs of oxidation, and its conductivity is much lower than that of all other samples, with a difference of ~3 log units at T< 1800 K relative to commercial CaS (**Figure 5**). The coulombic attraction between Ca^{2+} and O^{2-} being higher than Ca^{2+} and S^{2-} due to the larger ionic radius of sulfide, the mobility of Ca^{2+} or other cations is expected to decrease as S^{2-} is substituted for O^{2-}. As a result, conductivity decreases with increasing oxidation. We note that the small amount of C in the lab-synthesized CaS (**Figure 2**) is evidently too low to counteract the effects of oxidation for this oxidized sample.

The jump in conductivity as well as the associated change in the shape of impedance spectra (**Figure 4**) are consistent with melting. However, at 5 GPa, the temperatures at which this sharp increase occurs for the commercial CaS sample and the MgS sample (~2100 and 2050 K, respectively) are noticeably lower than the melting temperatures that are known for the endmembers at 1 atm (>2270 K; e.g., Egami et al., 1981; Ropp, 2013). Impurities are known to affect the melting properties of materials, especially by lowering the melting point. The low melting temperatures observed for these two endmembers likely reflect the presence of species such as Al, Mo, or Ta, alkali metals in the commercial CaS, or carbon in the lab-synthesized MgS.

The electrical conductivity of our samples under GPa-level pressures tends to be higher than at 1 atm (**Figure 5**). Variation of pressure between 2 – 6 GPa shows two trends. For the lab-synthesized CaS and $Ca_{0.2}Mg_{0.8}S$, increasing pressure decreases conductivity. For commercial CaS, data at 3 and 5 GPa are comparable, but conductivity values at 6 GPa are slightly higher than at lower pressure. As a whole, the pressure dependence is complex and likely involves multiple influences, including changes in inter-grain transport, differences in annealing (note that the

501 previous experiments at 3 and 6 GPa were not annealed), and competing effects of ionic vs.
502 electronic mechanisms that depend on the types of impurities and temperature. Further work on
503 the pressure dependence of conductivity is needed to unravel the effects of annealing and
504 impurities.
505 In addition to chemistry, textural effects influence the sulfide conductivity. At temperatures
506 below ~1500 K, the electrical conductivity of the samples spans a large range of values (up to 3
507 log units at 1100 K and 5 GPa). All starting materials are powders that have been annealed at
508 variable temperature and duration that were necessary to reach a stable electrical response. The
509 stabilization in bulk resistance indicates that a certain degree of textural and chemical equilibrium
510 was achieved at a specific temperature (Tauber et al., 2023). If a different annealing temperature
511 or time were selected, different grain sizes or distribution of impurities would be a likely outcome,
512 thereby affecting bulk conductivity. Longer annealing times or higher temperatures than what we
513 report here were avoided because these conditions would have oxidized the samples significantly.
514 As discussed below (section 4.3), the application of our electrical data to the field focuses
515 essentially on high temperatures (>1500 K), where the effect of the annealing conditions on
516 conductivity becomes small or negligible. At T>1500 K and until the jump in conductivity, the
517 values for all samples (except lab-synthesized CaS) tend to converge and show only slight
518 temperature dependence.
519 To summarize, the electrical results suggest evidence against simple ionic conduction in
520 our impurity-bearing sulfide samples. The measured conductivity is a complex interplay between
521 contributions from 1) the variety of charge carriers, i.e., alkaline earth cations (Ca^{2+}, Mg^{2+}) and
522 electronic defects related to the presence of impurities (mainly Na^{+} and C); 2) textural effects
523 (grain growth, and at high temperature, melting); 3) minor contamination from cell parts (Al, Ta
524 or Mo) at high temperature. Oxidation affected the lab-synthesized CaS sample, resulting in
525 anomalously low conductivities that are excluded from the discussion below. Our work does not
526 support the use of pure alkaline earth sulfides as analogs of natural, impurity-bearing samples
527 because impedance spectroscopy is highly sensitive to the presence of trace elements.
528
529 *4.3. Electrical conductivity-depth profiles of Mercury's mantle*
530 Given the sensitivity of electrical conductivity to temperature and composition, the
531 electrical conductivity-depth profile of the planet can be used to provide insights about the interior

of Mercury (Verhoeven et al., 2009; Genova et al., 2021). In this section, we propose electrical conductivity-pressure profiles of a sulfide-bearing Mercury mantle (**Figure 6**). Calculations are based on the results from this study for alkaline earth sulfide aggregates containing less than 1 vol.% graphite. These models can be tested with future induction data about the interior of the planet from the Bepi-Colombo mission (Heyner et al., 2021).

Our experimental results (**Figure 5**) show that impurity-bearing $Ca_{1-x}Mg_xS$ can be more conductive (>1 S/m) at a given temperature in the range T>1400-1500 K than a partially molten silicate matrix (conductivity typically < 1 S/m; e.g., Yoshino et al., 2010). Therefore, if the amount of sulfide in the silicate mantle of Mercury exceeds the percolation threshold, sulfide would increase bulk rock conductivity. This percolation threshold is not known for (Ca,Mg)S compositions, but has been found to be 6–8 vol.% for FeS in an olivine-rich matrix at comparable pressure and temperature conditions (Yoshino et al., 2003, 2004; Watson and Roberts, 2011; Tauber et al., 2023). Similar amounts of alkaline earth sulfides can be expected in Mercury (e.g., Stockstill-Cahill et al., 2012; Vander Kaaden et al., 2017). Despite the non-wetting behavior of sulfides in a silicate matrix (e.g., Marrocchi and Libourel, 2013), a partial sulfide network is sufficient to affect conductivity significantly if the content exceeds the percolation threshold (Tauber et al., 2023). The estimated temperature-depth profile of Mercury's present-day mantle (e.g., Knibbe and van Westrenen, 2018; Steinbrügge et al., 2021; Davies et al., 2024; **Figure 6a**) indicates that T is possibly higher than 1400 K over most of the mantle (P> ~1.1 GPa), implying that the conductivity of alkaline earth sulfides is expected to be higher than that of silicate minerals in the range ~1−5 GPa. In addition, this temperature-depth profile indicates that C-bearing sulfides could be molten (with conductivity values >10 S/m; **Figure 5**) in approximately the lower half of the mantle (~2.5−5GPa). Without the presence of impurities, especially carbon, it is expected that $Ca_{1-x}Mg_xS$ would not melt until higher temperatures are reached, and thus, could be solid in the entire mantle.

Bulk rock conductivity with a variable degree of sulfide interconnectivity can be computed using mixing models (Glover, 2015 and references therein). Experimental petrology studies on analogs of Mercury's surface suggested that the silicate mantle is likely heterogenous in composition (Charlier et al., 2013; Weider et al., 2015; Namur et al., 2016b; McCoy et al., 2018). In particular, lherzolite and harzburgite sources have been invoked to explain the mineralogy of different terranes (Charlier et al., 2013). As a result, the silicate mantle composition considered in

563 the calculations is lherzolitic or harzburgitic, corresponding to different mixtures of olivine
564 (forsterite), orthopyroxene (enstatite), and clinopyroxene (diopside). Using our electrical results
565 on sulfides, previous electrical studies on silicate minerals, and the present-day thermal profile in
566 **Figure 6a**, electrical conductivity-depth profiles of the mantle are calculated for varying sulfide
567 content and connectivity. The electrical conductivity of the sulfide phase is that of the $Ca_{0.2}Mg_{0.8}S$
568 sample because this composition is close to estimates from Stockstill-Cahill et al. (2012) ($Ca_{0.26-0.21}Mg_{0.74-0.79}S$).
569 The conductivity of forsterite, enstatite, and diopside are from Yoshino et al.
570 (2017), Zhang et al. (2012), and Zhao and Yoshino (2016), respectively (**Supplementary**
571 **Information**). Electrical data from these previous studies were collected at pressures and
572 temperatures that did not cover entirely the ranges for the mantle. Therefore, when needed, the
573 conductivity values have been extrapolated to relevant temperature conditions using the Arrhenius
574 equation for the specific mineral. The pressure dependence of conductivity being limited for the
575 considered silicate minerals over the range spanned by the mantle (~5 GPa), a correction was not
576 applied to electrical data from studies that did not provide a pressure dependence.

577 Bulk conductivity of the sulfide-free (**Figure 6b**) and sulfide-bearing (**Figure 6c**) mantle
578 is computed using the geometric mean

579 $$\sigma_{bulk} = \prod_{i=1}^{n} \sigma_i^{X_i} \quad (4)$$

580 with σ_i and X_i being the conductivity of phase i (i.e., olivine, orthopyroxene, clinopyroxene +/-
581 sulfide) and the volume fraction of phase i, respectively. This model considers arbitrary shaped
582 and randomly distributed phases (Glover, 2015), i.e., the sulfide phase is not interconnected. The
583 different mineralogies present comparable electrical conductivity values along the thermal profile
584 of the mantle. For each composition, conductivity increases with increasing temperature, therefore
585 with increasing depth as well. The addition of sulfide distributed randomly increases bulk
586 conductivity. For instance, at 1000 K, the presence of 10 vol.% sulfide increases mantle
587 conductivity by a factor of 2.6. At the bottom of the mantle, conductivity increases by a factor of
588 1.4 to 3.5 when 5 to 20 vol.% of randomly distributed sulfide is added.

589 The conductivity of a mantle with a varying connectivity of alkaline earth sulfide (**Figure**
590 **6d**) is calculated using the modified Archie's law (Glover et al., 2000)

591 $$\sigma_{bulk} = \sigma_{silicate}(1 - X_{sulfide})^p + \sigma_{sulfide} X_{sulfide}^m \text{ where } p = \frac{log\,(1-X_{sulfide}^m)}{log\,(1-X_{sulfide})} \quad (5)$$

592 with *m* the cementation exponent that is related to the electrical connectivity of the sulfide phase
593 in the silicate medium. Compared to other mixing models with variable exponents (e.g., Bussian
594 model), Eq. (5) reproduces experimental data satisfactorily (Glover et al., 2000). In Eq. (5), silicate
595 conductivity corresponds to that of a mantle composed of 70 vol.% forsterite and 30 vol.%
596 enstatite, obtained using the conductivity of each mineral and the geometric mean (Eq. 4). **Figure**
597 **6d** shows conductivity estimates for a mantle containing 8 vol.% sulfide. The cementation
598 exponent, *m*, is varied from 1 to 5, the high values implying poor interconnectivity of the sulfide
599 phase. Increasing the connectivity of the sulfide phase increases bulk conductivity significantly.
600 For instance, at a depth of 2 GPa, corresponding to a temperature estimate of 1750 K, decreasing
601 the cementation exponent from 5 to 1 increases bulk conductivity by a factor of ~5 (from 2.10^{-2} to
602 ~10^{-1} S/m). In addition, a CMB region with interconnected alkaline earth sulfides would be
603 characterized by high conductivity values (>8 S/m).
604 The electrical conductivity-depth profile of Mercury's mantle has been previously
605 estimated, and a comparison with our results is shown in **Figure 6d**. Verhoeven et al. (2009)
606 considered six silicate compositions with different mineralogies (five compositions are iron-poor,
607 one is Moon-like) and two temperature profiles (Buske, 2006; Spohn, 1991) spanning a large
608 temperature range (~1600-1950 K) in the lower part of the mantle. The T estimates in the mantle
609 are in broad agreement with the thermal profile used in our study (**Figure 6a**). However, one major
610 difference between this previous study and our calculations is that a significant amount of garnet
611 and coesite or periclase is considered in the models by Verhoeven et al. (2009) (>15 vol.%). In
612 addition, the Arrhenius equations used to compute the conductivity of olivine and orthopyroxene
613 (their Table 2) are significantly different from the laboratory-based equations used in our
614 calculations (**Supplementary material**). Because of the diversity of compositions considered,
615 Verhoeven et al. (2009) predicted large ranges of mantle conductivity. Their estimates show low
616 mantle conductivity values compared to our estimates, but our conductivity values for a sulfide-
617 free mantle or a sulfide-bearing mantle with poor interconnectivity of the sulfide phase are in good
618 agreement with their enstatite chondrite mineralogy (**Figure 6d**). The magnetic observations from
619 the MESSENGER mission were used to develop a simple radial conductivity model (Johnson et
620 al., 2018). The model assumes a strong conductivity increase with depth in the top part of the
621 mantle, in agreement with our estimates, and a constant conductivity value of 0.1 S/m across most

of the mantle (**Figure 6d**). Future measurements as part of the Bepi-Colombo mission will help constrain the interior of Mercury using electrical conductivity.

Further laboratory studies of the physical properties (thermal conductivity, viscosity, density) of alkaline earth sulfides under pressure and temperature are needed to improve models of the dynamics and evolution of the planet, as well as to interpret field observations from space missions. As an example, in the evolutionary model of Davies et al. (2024) that considers a silicate mantle and a Fe-Si core, the low density of CaS and MgS (varying from ~2.6 g/cm^3 at 500 K and 0.1 GPa to 2.9 g/cm^3 at 2100 K and 5 GPa, using the equation of state from Peiris et al. (1994) and references therein) lowers the bulk density of the mantle. This observation suggests that if Mercury contains significant amounts of CaS−MgS, the moment of inertia of the planet can only be satisfied by a smaller and denser core compared to the core of a planet without sulfide in its mantle. In terms of composition, increasing the density of the core is achieved by decreasing its amount of Si (<12 wt.%). Additional density measurements are needed on intermediate $Ca_{1-x}Mg_xS$ compounds to develop a density-depth profile of the mantle and investigate its effect on core composition.

5. Conclusions

We investigated the electrical properties of impurity-bearing alkaline earth sulfides in the CaS–MgS system, synthesized under vacuum in graphite capsules at 1473 K, and of commercial CaS. Our results from electrical experiments at 2 and 5 GPa show that conductivity increases with temperature, with activation energy values in agreement with alkaline earth cations and impurities (alkali, C) being the main charge carriers. No systematic effect of composition on conductivity is observed, which is likely caused by the effect of impurities. For all samples, *in situ* impedance measurements are relevant to detect the onset of melting, which was found to vary between ~1850 and 2100 K at 5 GPa. The presence of small amounts (tens to hundreds of ppm) of impurities (mostly, C for samples synthesized in graphite capsules, alkali for commercial CaS, and for all samples at high temperature, possibly Al, Mo or Ta) increases conductivity significantly and decreases the melting temperature, consistent with previous observations at 1 atm. Electrical conductivity can be high (>1 S/m) for molten sulfides containing impurities. In contrast, alteration (oxidation) of CaS results in a large decrease in conductivity.

Combining our results with petrological studies of Mercury's mantle and previous electrical studies of silicate minerals, we proposed different electrical conductivity-depth profiles of a sulfide-bearing mantle, varying the amount and connectivity of alkaline earth sulfides. At the bottom of the mantle, conductivity can be > 8 S/m if the sulfide phase is well interconnected. These electrical profiles across the mantle of Mercury can be compared with future electromagnetic data from the ESA-JAXA Bepi-Colombo mission.

Acknowledgements. AP thanks Emma Bullock for her help with microprobe analyses, Vasilije Dobrosavljevic and Zachary Geballe for fruitful discussions, Anon Cadieux and M.A. O'Donnell for their help with the literature, and acknowledges support from the Carnegie Institution for Science.

Data availability statement

All electrical conductivity data collected in this study are available in the supplementary materials and will be available from Dryad after acceptance (DOI: 10.5061/dryad.nk98sf82m).

The following temporary link is available during the peer-review process:

https://datadryad.org/stash/share/0xo608LiDBpHaXD50uVAlZxHpKBsK8fNPjuR2AMvba8.

References

Anzures, B.A., Parman, S.W., Milliken, R.E., Namur, O., Cartier, C., Wang, S. (2020). Effect of sulfur speciation on chemical and physical properties of very reduced mercurian melts. Geochimica et Cosmochimica Acta, 286, 1–18. https://doi.org/10.1016/j.gca.2020.07.024

Avril, C., Malavergne, V., Caracas, R., Zanda, B., Reynard, B., Charon, E., Bobocioiu, E., Brunet, F., Borensztajn, S., Pont, S., Tarrida, M., Guyot, F. (2013). Raman spectroscopic properties and Raman identification of CaS-MgS-MnS-FeS-Cr_2FeS_4 sulfides in meteorites and reduced sulfur-rich systems. Meteoritics and Planetary Science, 48, 1415–1426. https://doi.org/10.1111/maps.12145

683 Boukaré, C.E., Parman, S.W., Parmentier, E.M., Anzures, B.A. (2019). Production and
684 preservation of sulfide layering in Mercury's mantle. Journal of Geophysical Research:
685 Planets, 124, 3354–3372. https://doi.org/10.1029/2019JE005942
686 Buchanan, M., Haberkorn, R., Bilz, H. (1974). Second-order Raman effect in alkaline earth oxides.
687 Journal of Physics C: Solid State Physics, 7, 439 – 444.
688 https://doi.org/10.1088/0022-3719/7/2/022
689 Burbine, T.H., McCoy, T.J., Nittler, L. R., Benedix, G.K., Cloutis, E. A., Dickinson, T.L. (2002).
690 Spectra of extremely reduced assemblages: Implications for Mercury. Meteoritics and
691 Planetary Science, 37, 1233–1244. https://doi.org/10.1111/j.1945-5100.2002.tb00892.x
692 Buske, M. (2006). Dreidimensionale thermische Evolutionsmodelle für das Innere von Mars and
693 Merkur. PhD thesis. Göttingen.
694 Cartier, C., and Wood, B.J. (2019). The role of reducing conditions in building Mercury. Elements,
695 15, 39-45. https://doi.org/10.2138/gselements.15.1.39
696 Charlier, B., Grove, T.L., Zuber, M.T. (2013) Phase equilibria of ultramafic compositions on
697 Mercury and the origin of the compositional dichotomy. Earth and Planetary Science, 363, 50-
698 60. https://doi.org/10.1016/j.epsl.2012.12.021
699 Collins, B.T., and Ling, M. (1993). Synthesis and cathodoluminescence of orange-yellow to red-
700 emitting $Ca_{1-x}Mg_xS$:Mn phosphors. Journal of Electrochemical Society, 140, 1752–1755.
701 https://doi.org/10.1149/1.2221636
702 Crozaz, G., and Lundberg, L.L. (1995). The origin of oldhamite in unequilibrated enstatite
703 chondrites. Geochimica et Cosmochimica Acta, 59, 3817–3831.
704 https://doi.org/10.1016/0016-7037(95)00268-5
705 Davies, C., Pommier, A., Greenwood, S., Wilson, A. (2024). Thermal and magnetic evolution of
706 Mercury with a layered Fe-Si(-S) core. Earth and Planetary Science Letters, 641, 118812.
707 https://doi.org/10.1016/j.epsl.2024.118812
708 Dilner, D. (2016). Thermodynamic description of the Fe–Mn–Ca–Mg–S system. CALPHAD:
709 Computer Coupling of Phase Diagrams and Thermochemistry, 53, 55–61.
710 https://doi.org/10.1016/j.calphad.2016.03.005
711 Dyal, P., and Parkin, C.W. (1971). Electrical conductivity and temperature of the lunar interior
712 from magnetic transient-response measurements. Journal of Geophysical Research, 76, 5947–
713 5969. https://doi.org/10.1029/JA076i025p05947

714 Egami, A., Onoye, T., Narita, K. (1981). Electrical conductivities of alkaline earth sulfides.
715 Transactions of the Japan Institute of Metals, 22, 399-409.
716 https://doi.org/10.2320/matertrans1960.22.399
717 Farrell, S.P., Fleet, M.E., Stekhin, I.E., Kravtsova, A., Soldatov, A.V., Liu, X. (2002). Evolution
718 of local electronic structure in alabandite and niningerite solid solutions [(Mn,Fe)S, (Mg,Mn)S,
719 (Mg,Fe)S] using sulfur K- and L-edge XANES spectroscopy. American Mineralogist, 87, 1321
720 – 1332. https://doi.org/10.2138/am-2002-1007
721 Frost, R.L., and Keeffe, E.C. (2009). Raman spectroscopic study of the sulfite-bearing minerals
722 scotlandite, hannebachite, and orschallite: implications for the desulfation of soils. Journal of
723 Raman Spectroscopy, 40, 244–248. https://doi.org/10.1002/jrs.2089
724 Genova, A., Hussmann, H., Van Hoost, T., Heyner, D., Iess, L., Santoli, F., Thomas, N., Cappuccio,
725 P., de Stefano, I., Kolhey, P., Langlais, B., Mieth, J.Z.D., Oliveira, J.S., Stark, A., Steinbrügge,
726 G., Tosi, N., Wicht, J., Benkhoff, J. (2021). Geodesy, geophysics and fundamental physics
727 investigations of the BepiColombo mission. Space Science Reviews, 217, 31.
728 https://doi.org/10.1007/s11214-021-00808-9
729 Glover, P.W.J. (2015). Geophysical Properties of the Near Surface Earth: Electrical Properties,
730 Treatise on Geophysics 2nd edition, 89–137.
731 https://doi.org/10.1016/B978-0-444-53802-4.00189-5
732 Glover, P.W.J., Pous, J., Queralt, P., Muñoz, J.-A., Liesa, M., Hole, M.J. (2000). Integrated two-
733 dimensional lithospheric conductivity modelling in the Pyrenees using field-scale and
734 laboratory measurements. Earth and Planetary Science Letters, 178, 59–72.
735 https://doi.org/10.1016/S0012-821X(00)00066-2
736 Gyakwaa, F., Aula, M., Alatarvas, T., Vuolio, T., Shu, Q., Huttula, M., Fabritius, T. (2020).
737 Application of Raman spectroscopy for characterizing synthetic non-metallic inclusions
738 consisting of calcium sulphide and oxides. Applied Sciences, 10, 2113.
739 https://doi.org/10.3390/app10062113
740 Heyner, D., Auster, H.-U., Fornaçon, K.-H., Carr, C., Richter, I., Mieth, J.Z.D., Kolhey, P., Exner,
741 W., Motschmann, U., Baumjohann, W., Matsuoka, A., Magnes, W., Berghofer, G., Fischer, D.,
742 Plaschke, F., Nakamura, R., Narita, Y., Delva, M., Volwerk, M., Balogh, A., Dougherty, M.,
743 Horbury, T., Langlais, B., Mandea, M., Masters, A., Oliveira, J.S., Sánchez-Cano, B., Slavin,
744 J.A., Vennerstrøm, S., Vogt, J., Wicht, J., Glassmeier, H. (2021). The BepiColombo planetary

magnetometer MPO-MAG: What can we learn from the Hermean magnetic field? Space Science Reviews, 217, 52. https://doi.org/10.1007/s11214-021-00822-x

Hofmeister, A.M., Keppel, E., Speck, A.K. (2003). Absorption and reflection infrared spectra of MgO and other diatomic compounds. Monthly Notices of the Royal Astronomical Society, 345, 16 – 38. https://doi.org/10.1046/j.1365-8711.2003.06899.x

Jha, P., Sakalle, U.K., Sanyal, S.P. (1998). Pressure induced structural phase transition in MgS and CaS. Journal of Physics and Chemistry of Solids, 59, 599–603. https://doi.org/10.1016/S0022-3697(97)00245-X

Johnson, C.L., Anderson, B.J., Korth, H., Phillips, R.J., Philpott, L.C. (2018). Mercury's internal magnetic field. In Mercury, the View After MESSENGER. Cambridge University Press, 114–143. https://doi.org/10.1017/9781316650684.006

Kasano, H., Megumi, K., Yamamoto, H. (1984). Cathodoluminescence of $Ca_{1-x}Mg_xS$: A (A = Eu or Ce). Journal of the Electrochemical Society, 113, 1953 – 1960. https://doi.org/10.1149/1.2115999

Khurana, K.K., Jia, X., Kivelson, M.G., Nimmo, F., Schubert, G., Russell, C.T. (2011). Evidence of a global magma ocean in Io's interior. Science, 332, 1186–1189. https://doi.org/10.1126/science.1201425

Kivelson, M.G., Khurana, K.K., Russell, C.T., Volwerk, M., Walker, R.J., Zimmer, C. (2000). Galileo magnetometer measurements: A stronger case for a subsurface ocean at Europa. Science, 289, 1340–1343. https://doi.org/10.1126/science.289.5483.1340

Klein, C. and Hurlbut Jr., C. S. (1999). Manual of Mineralogy (after James D. Dana), 21st edition revised, Wiley, p. 188.

Knibbe, J.S., and van Westrenen, W. (2018). The thermal evolution of Mercury's Fe–Si core. Earth and Planetary Science Letters, 482, 147–159, doi:10.1016/j.epsl.2017.11.006

Lark, L.H., Parman, S., Huber, C., Parmentier, E.M., Head III, J.W. (2022). Sulfides in Mercury's mantle: Implications for Mercury's interior as interpreted from moment of inertia. Geophysical Research Letters, 49, e2021GL096713. https://doi.org/10.1029/2021GL096713

Lehner, S.W., Petaev, M.I., Zolotov, M.Yu, Buseck, P.R. (2013). Formation of niningerite by silicate sulfidation in EH3 enstatite chondrites. Geochimica et Cosmochimica Acta, 101, 34–56. https://doi.org/10.1016/j.gca.2012.10.003

775 Littleton, J. A. H., Secco, R. A., Yong, W. (2021). Electrical resistivity of FeS at high pressures
776 and temperatures: Implications of thermal transport in the core of Ganymede. Journal of
777 Geophysical Research: Planets, 126, e2020JE006793.
778 https://doi.org/10.1029/2020JE006793
779 Liu, Y. (2018). Raman, Mid-IR, and NIR spectroscopic study of calcium sulfates and mapping
780 gypsum abundances in Columbus crater, Mars. Planetary and Space Science, 163, 35–41.
781 https://doi.org/10.1016/j.pss.2018.04.010
782 Luo, H., Greene, R.G., Ghandehari, K., Li, T., Ruoff, A.L. (1994). Structural phase transformations
783 and the equations of state of calcium chalcogenides at high pressure. Physical Review B, 50,
784 16232 – 16237. https://doi.org/10.1103/PhysRevB.50.16232
785 Lutz, H.D., El Suradi, S. (1976). Zur Kenntnis der Calcium-, Strontium-, Barium-, Blei- und
786 Cadmiumsulfite. Spektroskopische, röntgenographische und thermoanalytische
787 Untersuchungen. Zeitschrift für anorganische und allgemeine Chemie, 425, 134-144
788 https://doi.org/10.1002/zaac.19764250207
789 Madarász, J., Leskelä, T., Rautanen, J., Niinistö, L. (1996). Oxidation of alkaline-earth-metal
790 sulfide powders and thin films. Journal of Materials Chemistry, 6, 781 – 787.
791 https://doi.org/10.1039/JM9960600781
792 Margot, J.-L., Hauck, S.A., Mazarico, E., Padovan, S., Peale, S.J. (2018). Mercury's internal
793 structure. In Mercury, the View After MESSENGER. Cambridge University Press, 85-113.
794 https://doi.org/10.1017/9781316650684.005
795 Marrocchi, Y., and Libourel, G. (2013). Sulfur and sulfides in chondrules. Geochimica et
796 Cosmochimica Acta, 119, 117–136. https://doi.org/10.1016/j.gca.2013.05.020
797 McCoy, T.J., Peplowski, P.N., McCubbin, F.M., Weider, S.Z. (2018). The geochemical and
798 mineralogical diversity of Mercury. In Mercury, the View After MESSENGER. Cambridge
799 University Press, 176–190. https://doi.org/10.1017/9781316650684.008
800 Mutschke, H., Begemann, B., Dorschner, J., Henning, Th. (1994). Infrared data of sulphides of
801 interstellar dust importance. Infrared Physics and Technology, 35, 361 – 374.
802 https://doi.org/10.1016/1350-4495(94)90094-9
803 Nagata, K., and Goto, K.S. (1974). Ionic conductivity of solid calcium sulfide at 650 to 1000 °C.
804 Metallurgical Transactions, 5, 899–903. https://doi.org/10.1007/BF02643145

805 Nakamura, H., and Gunji, K. (1980). Ionic conductivity of pure solid calcium sulfide. Transactions
806 of the Japan Institute of Metals, 21, 375–382.
807 https://doi.org/10.2320/matertrans1960.21.375
808 Nakamura, H., Ogawa, Y., Kasahara, A., Iwasaki, S. (1995). Sulfur pressure dependence of
809 electrical conductivity of Group IIa and IIIa metal sulfides. Materials Transactions, JIM, 36,
810 1263–1270. https://doi.org/10.2320/matertrans1989.36.1263
811 Namur, O., Charlier, B., Holtz, F., Cartier, C., McCammon, C. (2016a). Sulfur solubility in reduced
812 mafic silicate melts: Implications for the speciation and distribution of sulfur on Mercury. Earth
813 and Planetary Science Letters, 448, 102-114.
814 https://doi.org/10.1016/j.epsl.2016.05.024
815 Namur, O., Collinet, M., Charlier, B., Grove, T.L., Holtz, F., McCammon, C. (2016b). Melting
816 processes and mantle sources of lavas on Mercury. Earth and Planetary Science Letters, 439,
817 117-128. https://doi.org/10.1016/j.epsl.2016.01.030
818 Nemanich, R.J., Solin, S.A. (1979). First- and second-order Raman scattering from finite-size
819 crystals of graphite. Physical Review B, 20, 392 – 401.
820 https://doi.org/10.1103/PhysRevB.20.392
821 Ni, H., Keppler, H., Manthilake, M.A.G.M., Katsura, T. (2011) Electrical conductivity of dry and
822 hydrous $NaAlSi_3O_8$ glasses and liquids at high pressures. Contributions to Mineralogy and
823 Petrology, 162, 501-513. https://doi.org/10.1007/s00410-011-0608-5
824 Norby, T., Andersen, A.G. (1991). Electrical conductivity and defect structure of lithium-doped
825 magnesium oxide. Applied Catalysis, 71, 89 – 102.
826 https://doi.org/10.1016/0166-9834(91)85008
827 Ogawa, Y., Nakamura, H., Kasahara, A., Kodama, T. (1999). Ionic conductivity of CaS-Na_2S solid
828 solution. Materials Transactions, JIM, 40, 479–484.
829 https://doi.org/10.2320/matertrans1989.40.479
830 Pandey, R, and Sivaraman, S. (1991). Spectroscopic properties of defects in alkaline-earth sulfides.
831 Journal of Physics and Chemistry of Solids, 52, 211–225.
832 https://doi.org/10.1016/0022-3697(91)90066-9
833 Peiris, S.M., Campbell, A.J., Heinz, D.L. (1994). Compression of MgS to 54 GPa. Journal of
834 Physics and Chemistry of Solids, 55, 413–419.
835 https://doi.org/10.1016/0022-3697(94)90166-X

836 Peplowski, P.N., Klima, R.L., Lawrence, D.J., Ernst, C.M., Denevi, B.W., Frank, E.A., Goldsten,
837 J.O., Murchie, S.L., Nittler, L.R., Solomon, S.C. (2016). Remote sensing evidence for an
838 ancient carbon-bearing crust on Mercury. Nature Geoscience, 9, 273-276.
839 https://doi.org/10.1038/ngeo2669
840 Pommier, A. (2018). Influence of sulfur on the electrical resitivity of a crystallizing core in small
841 terrestrial bodies. Earth and Planetary Science Letters, 496, 37 – 46.
842 https://doi.org/10.1016/j.epsl.2018.05.032
843 Pommier, A., Leinenweber, K., Tran, T. (2019). Mercury's thermal evolution controlled by an
844 insulating liquid outermost core? Earth and Planetary Science Letters, 517, 125–134.
845 https://doi.org/10.1016/j.epsl.2019.04.022
846 Pommier, A., Tauber, M.J., Pirotte, H., Cody, G.D., Steele, A., Bullock, E.S., Charlier, B., Mysen,
847 B.O. (2023). Experimental investigation of the bonding of sulfur in highly reduced silicate
848 glasses and melts. Geochimica et Cosmochimica Acta, 363 114–128.
849 https://doi.org/10.1016/j.gca.2023.10.027
850 Reitze, M. P., Renggli, C., Morlok, A., Weber, I., Rodehorst, U., Berndt, J., et al. (2024).
851 Crystallographic and mid-infrared spectroscopic properties of the CaS-MgS solid solution.
852 Journal of Geophysical Research: Planets, 129, e2024JE008483.
853 https://doi.org/10.1029/2024JE008483
854 Renggli, C.J., Klemme, S., Morlok, A., Berndt, J., Weber, I., Hiesinger, H., King, P.L. (2022).
855 Sulfides and hollows formed on Mercury's surface by reactions with reducing S-rich gases.
856 Earth and Planetary Science Letters, 593, 117647. https://doi.org/10.1016/j.epsl.2022.117647
857 Renggli, C.J., Stojic, A.N., Morlok, A., Berndt, J., Weber, I., Klemme, S., Hiesinger, H. (2023).
858 Mid-infrared spectroscopy of sulfidation reaction products and implications for sulfur on
859 Mercury. Journal of Geophysical Research: Planets, 128, e2023JE007895.
860 https://doi.org/10.1029/2023JE007895
861 Rieder, K.H., Weinstein, B.A., Cardona, M., Bilz, H. (1973). Measurement and comparative
862 analysis of the second-order Raman spectra of the alkaline-earth oxides with a NaCl structure.
863 Physical Review B, 8, 4780 – 4786. https://doi.org/10.1103/PhysRevB.8.4780
864 Ropp, R.C. (2013). Group 16 (O, S, Se, Te) Alkaline Earth Compounds. Encyclopedia of the
865 alkaline earth compounds, 105-197, http://dx.doi.org/10.1016/B978-0-444-59550-8.00003-X

866 Salisbury, J.W., Walter, L.S., Vergo, N., D′Aria, D.M. (1991). Infrared (2.1 – 25 μm) Spectra of
867 Minerals. The Johns Hopkins Studies in Earth and Space Sciences, The Johns Hopkins
868 University Press.
869 Saxena, S., Pommier, A., Tauber, M.J. (2021). Iron sulfides and anomalous electrical resistivity in
870 cratonic environments. Journal of Geophysical Research: Solid Earth, 126 (9),
871 e2021JB022297. https://doi.org/10.1029/2021JB022297
872 Schmid, T., Jungnickel, R., Dariz, P. (2020). Insights into the $CaSO_4$-H_2O system: A Raman-
873 spectroscopic study. Minerals, 10, 115. https://doi.org/10.3390/min10020115
874 Schmid, T., Kraft, R., Dariz, P. (2021). Shedding light onto the spectra of lime – Part 2: Raman
875 spectra of Ca and Mg carbonates and the role of *d*-block element luminescence. Journal of
876 Raman Spectroscopy, 52, 1462 – 1472. https://doi.org/10.1002/jrs.6174
877 Skinner, B.J., and Luce, F.D. (1971). Solid solutions of the type (Ca, Mg, Mn, Fe)S and their use
878 as geothermometers for the enstatite chondrites. American Mineralogist, 56 (7-8), 1269–1296.
879 http://www.minsocam.org/ammin/AM56/AM56_1269.pdf
880 Sood, A.K., Gupta, R., Asher, S.A. (2001). Origin of the unusual dependence of Raman *D* band on
881 excitation wavelength in graphite-like materials. Journal of Applied Physics, 90, 4494 – 4497,
882 https://doi.org/10.1063/1.1408590
883 Spohn, T. (1991). Mantle differentiation and thermal evolution of Mars, Mercury and Venus. Icarus
884 90, 222–236. https://doi.org/10.1016/0019-1035(91)90103-Z
885 Steinbrügge, G., Dumberry, M., Rivoldini, A., Schubert, G., Cao, H., Schroeder, D. M., &
886 Soderlund, K. M. (2021). Challenges on Mercury's interior structure posed by the new
887 measurements of its obliquity and tides. Geophysical Research Letters, 48, e2020GL089895.
888 https://doi.org/10.1029/2020GL089895
889 Stockstill-Cahill, K.R., McCoy, T.J., Nittler, L.R., Weider, S.Z., Hauck II, S.A. (2012).
890 Magnesium-rich crustal compositions on Mercury: Implications for magmatism from
891 petrologic modeling. Journal of Geophysical Research: Planets, 117, E00L15,
892 https://doi.org/10.1029/2012JE004140
893 Tauber, M.J., Saxena, S., Bullock, E.S., Ginestet, H., Pommier, A. (2023). Electrical properties of
894 iron sulfide-bearing dunite under pressure: Effect of temperature, composition, and annealing
895 time. American Mineralogist, 108, 2193–2208. https://doi.org/10.2138/am-2023-9054

Vander Kaaden, K.E., McCubbin, F.M., Nittler, L.R., Peplowski, P.N., Weider, S.Z., Frank, E.A., McCoy, T.J. (2017). Geochemistry, mineralogy, and petrology of boninitic and komatiitic rocks on the mercurian surface: Insights into the mercurian mantle. Icarus, 285, 155–168. https://doi.org/10.1016/j.icarus.2016.11.041

Verhoeven, O., Tarits, P., Vacher, P., Rivoldini, A., Van Hoolst, T. (2009). Composition and formation of Mercury: Constraints from future electrical conductivity measurements. Planetary and Space Science, 57, 296–305. https://doi.org/10.1016/j.pss.2008.11.015

Vilas, F., Domingue, D.L., Helbert, J., D′Amore, M., Maturilli, A., Klima, R.L., Stockstill-Cahill, K.R., Murchie, S.L., Izenberg, N.R., Blewett, D.T., Vaughan, W.M., Head, J.W. (2016). Mineralogical indicators of Mercury's hollows composition in MESSENGER color observations, Geophys. Res. Lett., 43, 1450–1456. https://doi.org/10.1002/2015GL067515

Wallace, W.E. (retrieved in 2024). Infrared spectra in NIST Chemistry WebBook, NIST Standard Reference Database Number 69, Eds. P.J. Linstrom and W.G. Mallard, National Institute of Standards and Technology. https://doi.org/10.18434/T4D303 https://webbook.nist.gov/cgi/cbook.cgi?ID=B6000564&Units=SI&Mask=80#IR-Spec

Watson, H.C. and Roberts, J.J. (2011). Connectivity of core forming melts: Experimental constraints from electrical conductivity and X-ray tomography. Physics of the Earth and Planetary Interiors, 186, 172–182. https://doi.org/10.1016/j.pepi.2011.03.009

Weider, S.Z., Nittler, L.R., Starr, R.D., Crapster-Pregont, E.J., Peplowski, P.N., Denevi, B.W., Head, J.W., Byrne, P.K., Hauck II, S.A., Ebel, D.S., Solomon, S.C. (2015). Evidence for geochemical terranes on Mercury: Global mapping of major elements with MESSENGER's X-Ray Spectrometer. Earth and Planetary Science Letters, 416, 109-120. https://doi.org/10.1016/j.epsl.2015.01.023

Worrell, W.L., Tare, V.B., Bruni, F.J. (1969). Development of a high-temperature solid-sulphide electrolyte. Proceedings of the Third International Symposium on High Temperature Technology, IUPAC Publications, 503–509.

Yoshino, T. (2010). Laboratory Electrical Conductivity Measurement of Mantle Minerals. Surveys in Geophysics, 31, 163–206. https://doi.org/10.1007/s10712-009-9084-0

Yoshino, T., Walter, M.J., Katsura, T. (2003). Core formation in planetesimals triggered by permeable flow. Nature, 422, 154–157. https://doi.org/10.1038/nature01459

926 Yoshino, T., Walter, M.J., Katsura, T. (2004). Connectivity of molten Fe alloy in peridotite based
927 on in situ electrical conductivity measurements: Implications for core formation in terrestrial
928 planets. Earth and Planetary Science Letters, 222, 625–643.
929 https://doi.org/10.1016/j.epsl.2004.03.010
930 Yoshino, T., Zhang, B., Rhymer, B., Zhao, C., Fei, H. (2017), Pressure dependence of electrical
931 conductivity in forsterite. Journal of Geophysical Research: Solid Earth, 122, 158–171.
932 https://doi.org/10.1002/2016JB013555
933 Zhang, B., Yoshino, T., Wu, X., Matsuzaki, T., Shan, S., Katsura, T. (2012). Electrical conductivity
934 of enstatite as a function of water content: Implications for the electrical structure of the upper
935 mantle. Earth and planetary Science Letters, 357-358, 11–20.
936 http://dx.doi.org/10.1016/j.epsl.2012.09.020
937 Zhao, C., and Yoshino, T. (2016). Electrical conductivity of mantle clinopyroxene as a function of
938 water content and its implication on electrical structure of uppermost mantle. Earth and
939 Planetary Science Letters, 447, 1–9. https://doi.org/10.1016/j.epsl.2016.04.028

Table 1. Experimental conditions.

Experiment #	Sample	Electrode material	Pressure (GPa)	Quench T (K)
BBC61	CaS	Mo	5	2121
BBC64	CaS	Ta	2	1474
BBC86	Commercial CaS	Ta	5	2163
BB177*	Commercial CaS	Mo	6	2388
BB175*	Commercial CaS	Mo	3	1768
BBC81	$Ca_{0.8}Mg_{0.2}S$	Mo	5	1966
BBC85	$Ca_{0.8}Mg_{0.2}S$	Ta	2-5	1872
BBC79	$Ca_{0.6}Mg_{0.4}S$	Mo	5	1953
BBC82	$Ca_{0.4}Mg_{0.6}S$	Mo	5	1918
BBC83	$Ca_{0.2}Mg_{0.8}S$	Mo	2-5	2143
BBC80	MgS	Mo	5	2080

940 * Pommier et al., 2019.

941

Table 2. Summary of electron microprobe analyses (in wt.%).
Analyses of the starting materials are from Reitze et al. (2024).

	Samples	Mg	Ca	S	Ta	Mo	Al	Fe	Mn	Si	Na	Total
CaS	Starting material, not altered (4)	0.31 (0.02)[b]	55.2 (0.3)	43.9 (0.4)	-	-	-	-	-	-	-	99.3
	Starting material, altered (2)	0.26 (0.01)	49.8 (1.9)	38.8 (1.5)	-	-	-	-	-	-	-	88.8
	BBC61 (7)	0.08 (0.09)	54.7 (0.3)	42.7 (0.4)	0.00 (0.00)	0.08 (0.02)	0.00 (0.00)	0.00 (0.00)	0.00 (0.00)	0.01 (0.00)	0.02 (0.01)	97.6
	BBC64 (7)	0.18 (0.06)	54.4 (0.2)	42.8 (0.3)	0.00 (0.00)	0.09 (0.02)	0.01 (0.01)	0.00 (0.00)	0.00 (0.00)	0.02 (0.01)	0.03 (0.01)	97.6
$Ca_{0.8}Mg_{0.2}S$	Starting material (9)	7.49 (0.12)	46.3 (0.3)	46.3 (0.3)	-	-	-	-	-	-	-	100.1
	BBC81 (17)	2.82 (0.95)	51.3 (0.9)	41.6 (1.7)	0.00 (0.00)	0.12 (0.12)	0.02 (0.02)	0.02 (0.02)	0.00 (0.01)	0.14 (0.18)	0.02 (0.02)	96.0
$Ca_{0.6}Mg_{0.4}S$	Starting material (9)	14.6 (1.0)	37.1 (1.2)	48.5 (0.4)	-	-	-	-	-	-	-	100.1
	BBC67 (9)	13.5 (2.4)	38.0 (2.8)	45.6 (0.5)	0.05 (0.11)	0.08 (0.03)	0.02 (0.01)	0.05 (0.02)	0.01 (0.01)	0.03 (0.02)	0.05 (0.02)	97.4
	BBC79 (4)	10.0 (0.8)	41.7 (1.2)	43.4 (1.1)	0.00 (0.00)	0.09 (0.04)	0.01 (0.00)	0.06 (0.04)	0.01 (0.01)	0.03 (0.02)	0.07 (0.03)	95.3
$Ca_{0.4}Mg_{0.6}S$	Starting material (9)	22.6 (1.0)	26.6 (1.4)	50.7 (0.4)	-	-	-	-	-	-	-	99.9
	BBC82 (5)	15.4 (2.2)	34.7 (2.2)	45.8 (1.3)	0.00 (0.00)	0.10 (0.30)	0.01 (0.00)	0.05 (0.01)	0.00 (0.00)	0.03 (0.03)	0.09 (0.03)	96.1
$Ca_{0.2}Mg_{0.8}S$	Starting material (9)	33.5 (1.4)	12.8 (1.8)	54.2 (0.5)	-	-	-	-	-	-	-	100.5
	BBC83 (8)	33.0 (0.8)	14.2 (0.6)	52.4 (0.8)	0.00 (0.00)	0.10 (0.05)	0.07 (0.05)	0.00 (0.00)	0.00 (0.00)	0.01 (0.00)	0.01 (0.01)	99.8
MgS	Starting material (9)	43.1 (0.4)	0.46 (0.05)	56.1 (3.0)	-	-	-	-	-	-	-	99.7

[a] Number of analyses.
[b] Standard deviation.

942

943

944

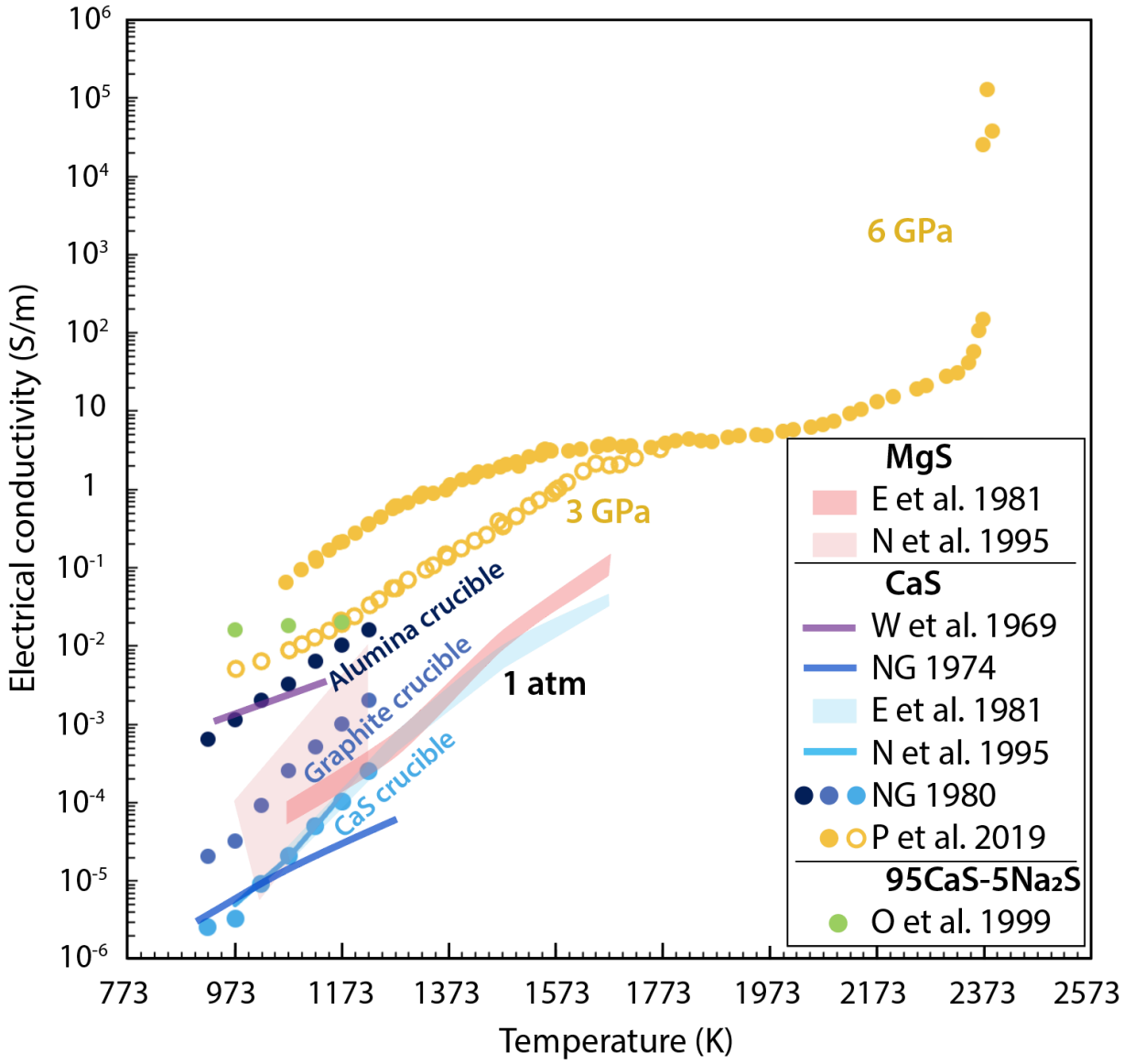

Figure 1: Electrical conductivity of CaS and MgS sulfides as a function of temperature from previous studies performed at 1 atm (W et al., 1969: Worrell et al., 1969; NG 1974: Nagata and Goto, 1974; NG 1980: Nakamura and Gunji, 1980; E et al.: Egami et al., 1981; N et al.: Nakamura et al., 1995; O et al.: Ogawa et al., 1999) and under pressure (P et al.: Pommier et al., 2019; Y-axis corrected relative to Fig. 3A of the original).

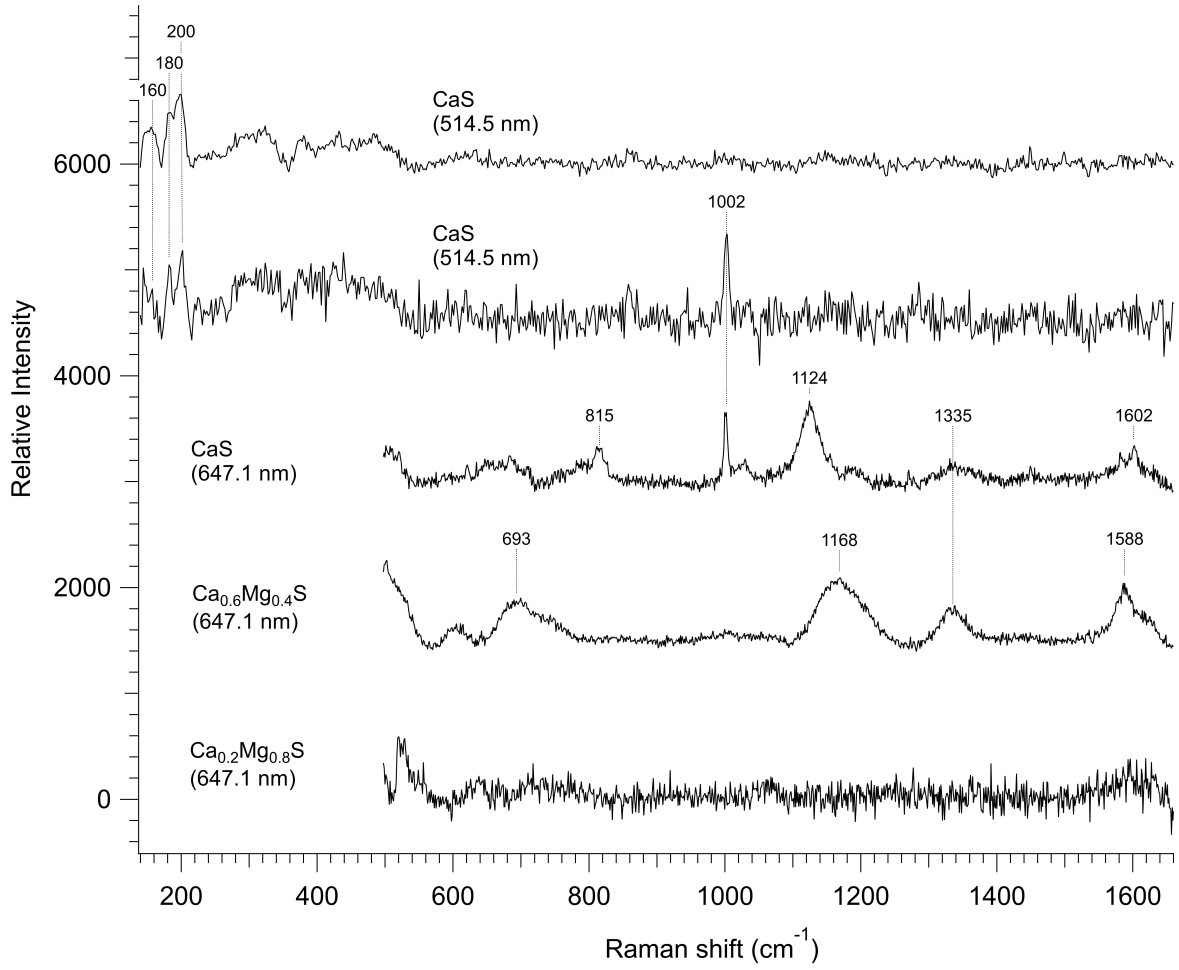

957

958 **Figure 2**: Raman spectra of representative sulfide samples, after removal of luminescence
959 backgrounds. The two upper spectra were acquired with 514.53-nm excitation, and probe two
960 different grains of CaS. The lower three spectra, acquired with 647.09-nm excitation and an
961 elliptical focus, cover the 500 – 1660 cm^{-1} range where bands of some impurities are anticipated.
962 Peak positions are labelled for those bands assigned to fundamental modes of CaS (160, 180, 200
963 cm^{-1}), sulfate (1002 cm^{-1}), and graphitic/sp^2 carbon (1335, 1588-1602 cm^{-1}). Additional bands with
964 labelled peak positions are likely due to luminescence from impurities (see text).

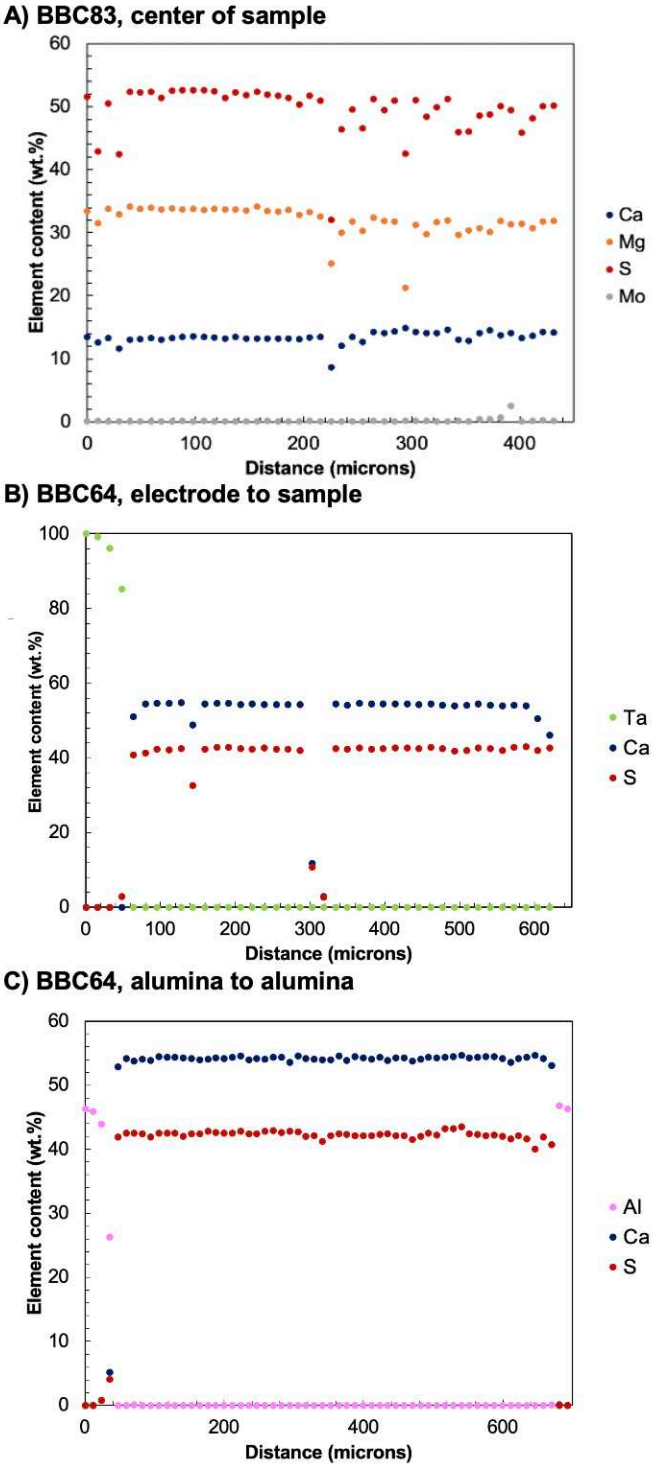

Figure 3: Electron microprobe traverses across samples BBC83 ($Ca_{0.8}Mg_{0.2}S$, with Mo electrodes), quenched at 2143 K (A) and BBC64 (CaS, with Ta electrodes), quenched at 1474 K and 2 GPa (B and C). Data points in the samples that are outliers correspond to analyses performed in areas with complicated textures (porosity, decompression cracks).

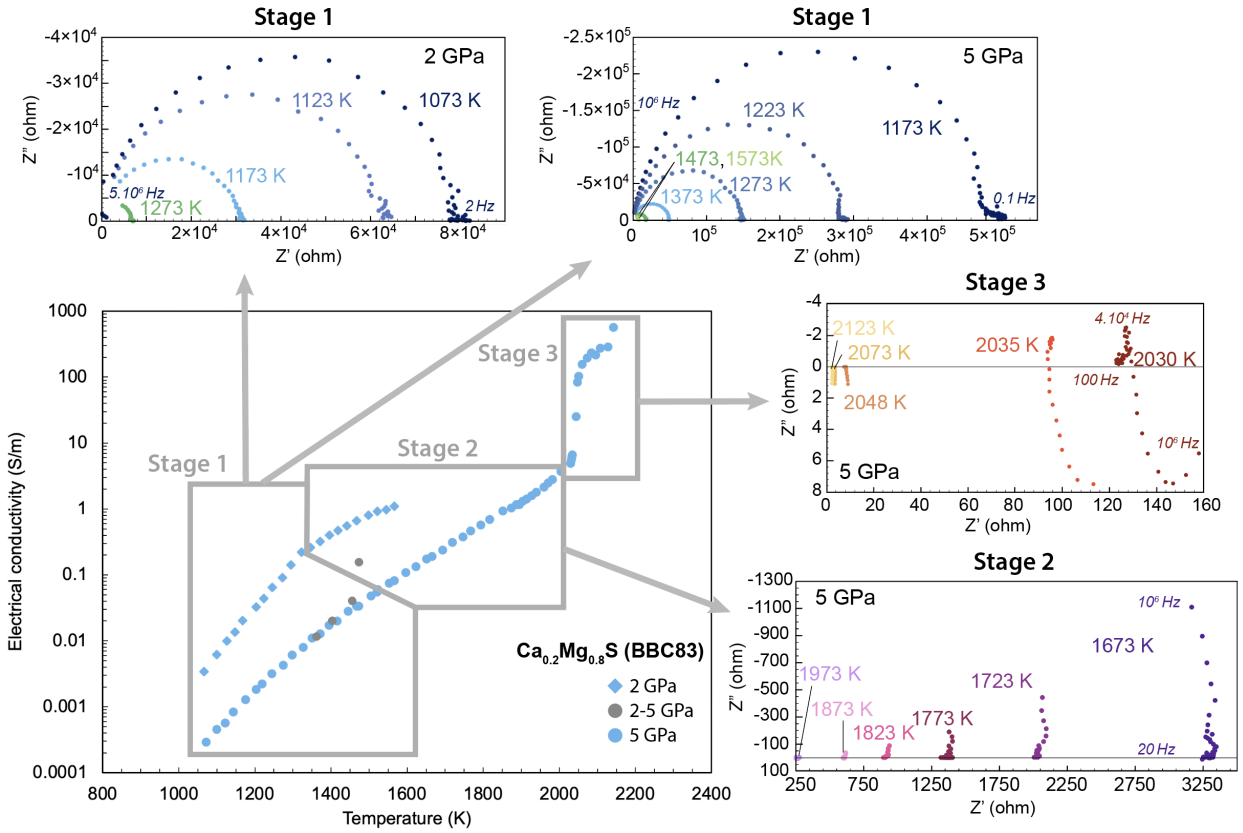

Figure 4: Electrical conductivity and impedance spectra as a function of temperature at 2 and 5 GPa for sample $Ca_{0.2}Mg_{0.8}S$ (experiment BBC83). Z' is the real part of impedance Z, and Z'' the imaginary part. In the conductivity plot, three stages can be identified. Blue diamonds and circles indicate data acquired at 2 and 5 GPa, respectively, and grey circles denote the data collected during the transition between the two pressures. For help with readability, the impedance plot for stage 3 shows a different scale for the Z' and Z'' axes. See text for details.

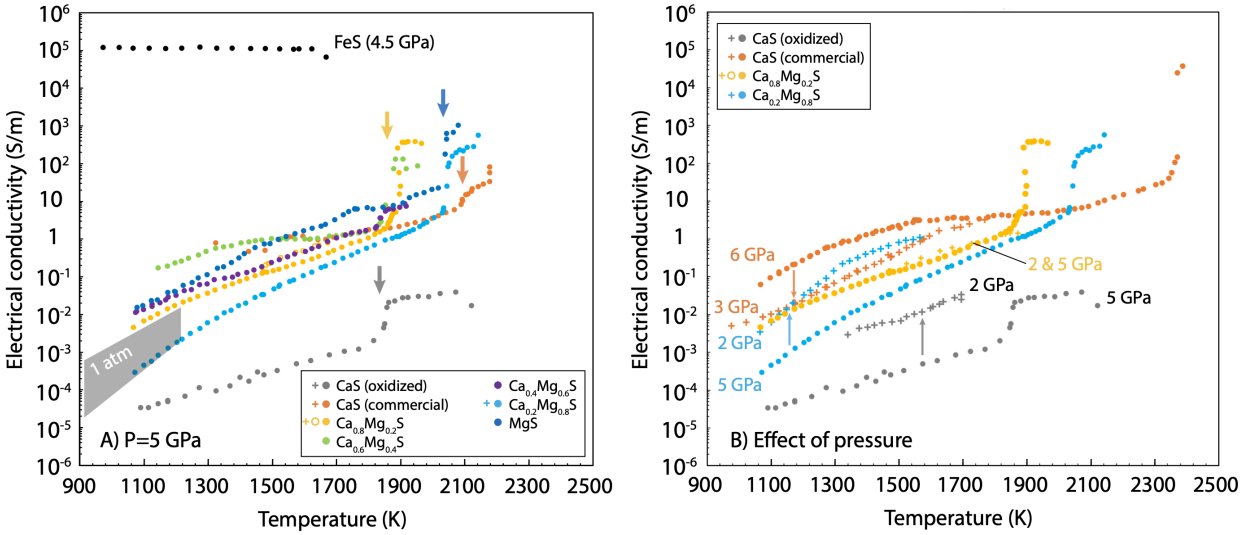

Figure 5: Electrical conductivity as a function of temperature for different pressures. A) Data at 5 GPa from this study. Vertical arrows indicate the electrical jump related to melting. Comparisons with previous data on FeS (Saxena et al., 2021; Pommier, 2018) and CaS at 1 atm (Nakamura and Gunji, 1980) are also shown. B) Effect of pressure on conductivity. Vertical arrows indicate the effect of a decrease in pressure. Data for commercial CaS at 3 and 6 GPa are from Pommier et al. (2019).

Figure 6 (next page): Thermal profile (A) and corresponding electrical conductivity-pressure profiles (B, C, and D) across the silicate portion of Mercury. A) Temperature from Davies et al. (2024). B) Conductivity- pressure profile of sulfide-free compositions (lherzolite/harzburgite). The conductivity of each silicate phase is from previous studies, and bulk conductivity is calculated using a geometric mean. C) Effect of sulfide content on the bulk conductivity of a silicate mantle (from B) made of 70 vol.% olivine (forsterite) and 30 vol.% orthopyroxene (enstatite). The conductivity of the sulfide phase is from this study ($Mg_{0.8}Ca_{0.2}S$), and bulk conductivity is calculated using a geometric mean. D) Effect of sulfide interconnectivity on the bulk conductivity of the silicate mantle shown in (C). 8 vol.% sulfide is considered, and bulk conductivity is calculated using the modified Archie's law. m corresponds to the cementation exponent. A value of 1 for cementation exponent m corresponds to an interconnected sulfide phase. Previous electrical conductivity estimates are also shown in (D) for comparison. The green dashed lines correspond to a simple radial conductivity model using magnetic observations from MESSENGER (Johnson et al., 2018). The grey area indicates the conductivity for different mantle mineralogies in the thermodynamic model of Verhoeven et al. (2009). The conversion of depth to pressure for the profiles of Verhoeven et al. (2009) and Johnson et al. (2018) was done using the Preliminary Reference Mercury Model by Margot et al. (2018).

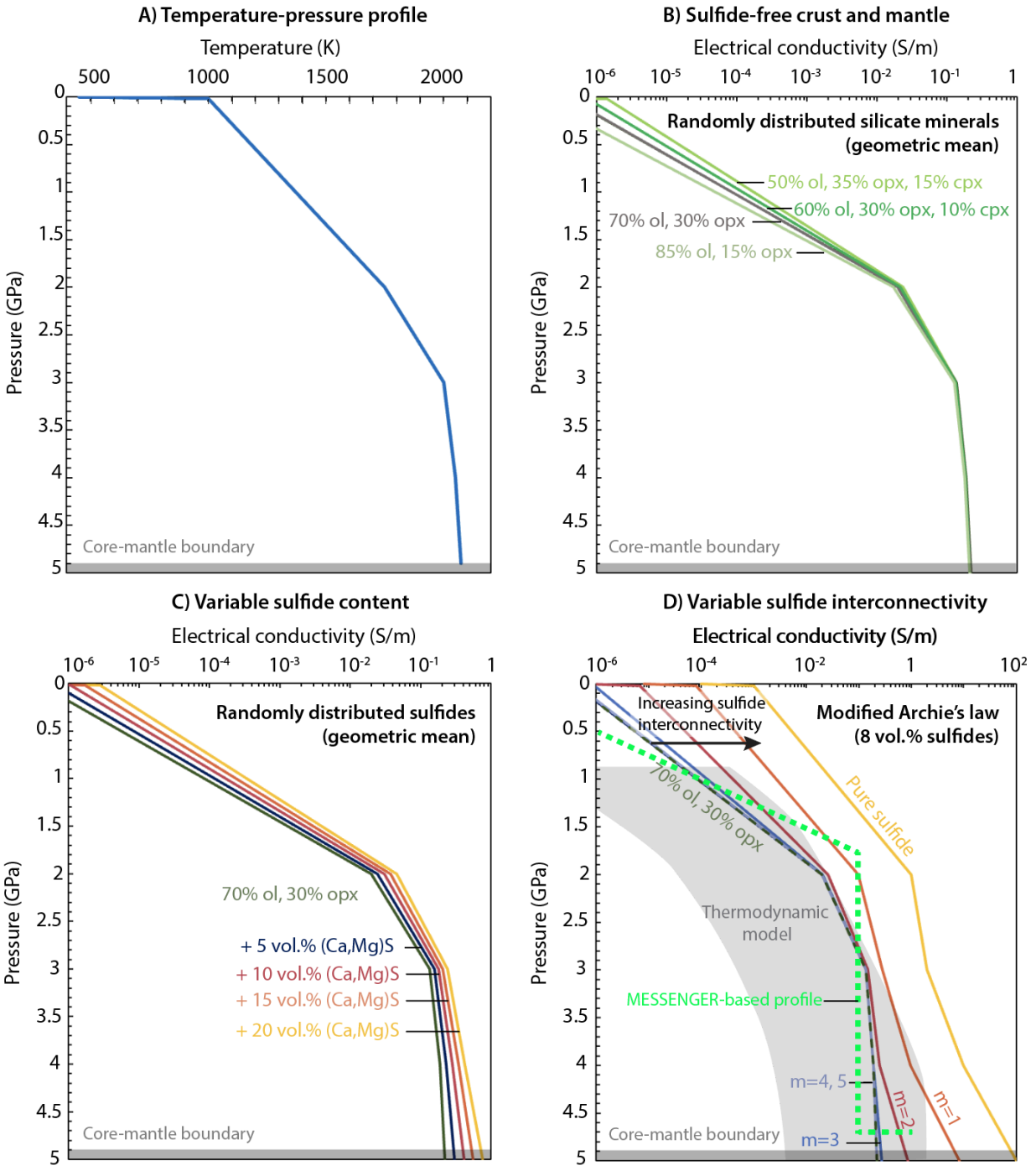
A) Temperature-pressure profile
Temperature (K)
500
1000
1500
2000
Pressure (GPa)
Core-mantle boundary
B) Sulfide-free crust and mantle
Electrical conductivity (S/m)
Randomly distributed silicate minerals
(geometric mean)
50% ol, 35% opx, 15% cpx
60% ol, 30% opx, 10% cpx
70% ol, 30% opx
85% ol, 15% opx
Core-mantle boundary
C) Variable sulfide content
Randomly distributed sulfides
(geometric mean)
70% ol, 30% opx
+ 5 vol.% (Ca,Mg)S
+ 10 vol.% (Ca,Mg)S
+ 15 vol.% (Ca,Mg)S
+ 20 vol.% (Ca,Mg)S
Core-mantle boundary
D) Variable sulfide interconnectivity
Increasing sulfide interconnectivity
Modified Archie's law
(8 vol.% sulfides)
Pure sulfide
70% ol, 30% opx
Thermodynamic model
MESSENGER-based profile
m=4, 5
m=2
m=1
m=3
Core-mantle boundary

1006